

Face Milling of Glass Fiber Reinforced Plastics (GFRP) with Chamfered Main Cutting Edge Carbide Tools

Chung-Shin Chang¹, Gwo-Chung Tsai²

¹ Professor, Department of Mechanical Engineering, National Ilan University

² Associate Professor, Department of Mechanical Engineering, National Ilan University

Abstract

Due to the special properties of composite materials, a reasonable analysis of the material response to milling with chamfered main cutting edge tool lacks progress yet. Knowledge acquired from metal cutting can be used only with care. In this study, the machinability of high-strength glass-fiber-reinforced plastics (GFRP) materials in face milling with chamfered main cutting edge of P and K type carbide tools have been investigated experimentally. Chip formation mechanisms and tool wear have been observed and the surface roughness has been measured with respect to tip's geometries and nose radii. A new force model for a single-point face milling cutters with a chamfered main cutting edge has been developed. The theoretical values of cutting forces were calculated and compared with the experimental results; the forces predicted by this model were consistent with the experimental values. A special tool holder and its geometry was designed and manufactured first, then these holders with the mounting tip's were grinded to various tool geometries, including the width of chamfered main cutting edge, the nose radii, the lead angle, first and second radial angle and axial angle... etc. In this paper, the sharp of chamfered main cutting edge tool induce decrease of the cutting force and the smallest of the cutting force values in the case of $C_s = 20^\circ$, $\alpha_{r1}(\alpha_{r2}) = -20^\circ(20^\circ)$. Comparing of the different P and K type of tools using in milling GFRP materials, K type of chamfered main cutting edge tool is better than P type of chamfered main cutting edge tool.

Key words : Face milling, glass fiber reinforced plastics (GFRP), chamfered main cutting edge, and build-up edge

負稜主刃銑刀加工玻璃纖維複材之研究

張充鑫¹ 蔡國忠²

¹ 國立宜蘭大學機械工程學系教授

² 國立宜蘭大學機械工程學系副教授

摘要

本研究是一種選用P型及K型材質的碳化物刀片，磨成負稜主刃銑刀後，針對玻璃纖維複合材料作切削研究。研究當中除了量測三軸切削力與預測值比較外，並觀察切屑的生成方式，刀片磨耗情形及工件表面光度等，結果顯示預測值與實驗值很接近。另外本研究在開始前，即先設計並製造出九種不同形狀的刀把，然後將刀片鎖在刀把上以磨成不同幾何形狀的刀片。此刀片包含負稜寬度，刀鼻半徑，導引角(lead angle)，第一與第二徑向角(radial angle)及軸向角(axial angle)，以作各種不同的實驗。實驗結果顯示，當導引角(C_s)一定，具有負稜的刀具切削力較低；且當 C_s 為 20° ，第一及第二徑向角， $\alpha_{r1}(\alpha_{r2})$ 分別為 $-10^\circ(10^\circ)$ 時，為一理想之刀具角度。另外K型負稜主刃面銑刀比P型面銑刀有較佳的切削效果。

關鍵詞:銀白色切屑, 玻璃纖維, 複合材料, 負稜主刃面銑刀

I. Introduction

Advanced fiber reinforced plastics composites (FRP) are being increasingly used in modern aerospace and other engineering applications. These materials and possibility of tailoring their performance mainly due to the high specific mechanical properties offer this [1]. Composite materials are ideal for structural applications where high strength-to-weight and stiffness-to-weight ratios are required [2]. Although these materials have higher strength characteristics and low density, the relatively lower elastic stiffness is observed. For this reason about 40 years ago experimental work was carried out on the thermal conversion of various organic precursor materials into carbon and graphite fibers and fabrics. By far the most common reinforcement for plastics in ablative and structural-composite applications was glass fibers. Glass-fiber-reinforced plastics (GFRP) has been successfully used in the aerospace, transportation, recreational, appliance, electrical equipment, tank and piping industries [3]. These materials wanted to be used in machine elements or aircraft structure, accurate surfaces for bearing mounting or adhesive joints must be provided to get precise machining. König et al. [4] presented in spite of the near net shape production technology available for the processing, molding and curing of fiber reinforced plastics; these materials have to be machined. Though components made of composite materials are often produced in their final forms, the removal of surplus materials for tolerance assurance of the components is required. Milling is the most convenient machining operation to achieve such a purpose [5]. The face milling process is one of the most widely used and efficient means of machining materials at relatively high metal removal rates. In this process there is a periodically varying chip section during the milling process, therefore the cutting force also vary during the process. The cutting efficiency increases significantly if the machine tool and the cutting tool are suitably selected. Suitable tools need sufficient hardness and to be of appropriate geometry. To this end, Kline and DeVor [6] have established a mechanistic end milling force model and implemented it on the computer. The machining of glass fiber-epoxy composite materials is not the same as the machining of conventional metal materials. The wear of sintered-carbide tools and high-speed steel tools is very severe. Hence the cutting speed and feed rate of the machining operation should be selected carefully in the machining of carbon fiber-epoxy composite materials. Also, surface damage of the composite materials such as cracking

II. Theoretical Analysis

Though composites have excellent performance characteristics, but when machined those tend to develop the following flaws: (1) surface delaminating: separation of plies where the cutter enters and exits the material; (2) internal delaminating: separation that develops between plies as a result of improper machining and drilling; (3) fiber/resin pullout: tearing away of fiber/resin from the wall of the machined edge; (4) high tool wear due to abrasion by hard

and delimitation of the machined surface is often observed and a low surface-roughness is not easily obtained [7, 8]. Machining characteristics of composites vary from metals due to the following reasons: (1) FRP is machinable in a limited range of temperature; (2) the low thermal conductivity causes heat build up in the cutting zone during machining operation, since there is only little dissipation by the materials; (3) the difference in the coefficient of linear expansion between the matrix and the fiber gives rise to residual stresses and makes it difficult to attain high dimensional accuracy; (4) the change in physical properties by the absorption of fluids has to be considered while deciding to use a coolant [1]. Due to the materials removal process is quite complex, many variables such as the workpiece material, the cutting tool material, the rigidity of the machine and the set up, the cutting feedrate and speed, tool wear, and chip control must be considered. Gallab [9] showed the cost of polycrystalline diamond tools (PCD) could be justified by using dry cutting; the relatively small built-up edge formed on the tool protects it from further wear by abrasion and micro cutting. The cutting efficiency would therefore significantly increase if a powerful machine tool and cutting tool were correctly selected. Kim and Ehmann [10] demonstrated the knowledge of the cutting forces is one of the most fundamental requirements. This knowledge also gives very important information for cutter design, machine tool design and detection of tool wear and breakage. Hoshi and Hoshi [11] found that the apparent strength and the life of tool were increased if a small region of negative rake angle was ground on the main cutting edge and the contact length was controlled by a chip curler. Hoshi [12] extensively studied the characteristics of the built-up edge (BUE) and developed a silver white chip tool in the milling method. This method involves tool geometries that produce a BUE which flows away continuously in the form of separated secondary chip. A tool of this type was reported to reduce the energy by 15% and prolong tool life by roughly 20% compared with conventional tools [13]. Chang [14] illustrated that face milling of medium carbon steel with chamfered main cutting edge tools could improve cutting efficiency. However, the effects of tool on face milling of the CFRP and GFRP were excluded from their discussion. The current paper presents a preliminary study on milling of on glass fiber/epoxy laminates using chamfered main cutting edge carbide tools. The effect of tool geometry, tool wear, chip formation and cutting force has been studied. Due to the time and the budget limit, some experiments had been performed to study the cases of GFRP material in milling with chamfered main cutting edge sharp tool, i.e. milling of GFRP with nose radius tool and milling of CFRP, the results of which will be presented in future.

fibers...etc. [1]. Since GFRP is difficult to machine, few researches had been found in the literature concerning of GFRP materials in milling with chamfered main cutting edge carbide tools. This study presents some experimental results to clarify details of GFRP composites in milling. Sreejith et al. [15] showed the wide difference in thermal properties of the fiber and matrix material and also the relatively poor thermal conductivity of composites make it rather difficult to adopt any of the unconventional technique for machining of the polymeric composites. Moreover, the shapes obtained by traditional turning, drilling, and unconventional processes cannot obtain related processes, and therefore traditional

material removed processes are the most suitable for machining polymeric composites. Composite materials are mainly molded parts, which require machining, especially face milling and surface turning, to obtain the desired dimensional tolerances, for achieving the desired quality of the machined surface, it is necessary to understand the mechanism of material removal, the kinetics of machining and the associated tribological processes affecting the performance of the cutting tools. Since available data on the machining of such materials are relatively few and inconclusive, a detailed machining study was contemplated. Wang et al. [16] illustrated in chip formation, cutting forces, and the surface morphology in edge trimming of unidirectional graphite/epoxy was highly dependent on fiber orientation. The chip's machined surface is defined as the surface in contact with the tool rake face, whereas the separated chip surface is the plane of chip discontinuity similar to the shear plane in metal cutting. Bhatnagar et al. [17] showed that on the machining of fiber reinforced plastic (FRP) composite laminates; it can be assumed that the shear plane in the matrix will depend only on the fiber orientation and not on the tool geometry.

Generally GFRP are heat insulating and abrasive in nature; hence the cutting tools have to encounter a relatively more hazardous environment and undergo thermal associated wear processes. The available reports on cutting temperature and associated influences are mostly related to applications involving chamfered main cutting edge carbide tools. The oblique cutting parameters predicted by the tool geometry and either of maximum shear stress or minimum energy principle is in good agreement with experimental data published in the literature from Shamoto and Altintas [18]. To obtain adequate strength of the cutting edge and to diminish the cutting forces, Hoshi & Hoshi [11] suggested that the value of the side rake(radial) angle α_2 should be in the range of

15° to 30° . Coefficients of the tool having a sharp corner ($R=0$) without tool wear and they modified the main cutting edge with a chamfer which had a negative primary side rake angle (α_1) of -30° and a suitable width W_e . The width W_e was constrained by the empirical equation (1).

$$W_e \cdot \cos C_s \leq f, \quad (1)$$

where f is the feedrate and C_s is the lead angle (side cutting edge angle)

According to Chang and Fuh [19], the chamfered main cutting edge tool which can produce a secondary chip reduces the cutting force and aids the thermal dissipation. The results indicated that, for ease of chip flow, the lead angle C_s should fall in the range of 20° to 40° . The first radial angle α_{r1} and the second radial angle α_{r2} are fall into the range of -10° to -30° and 10° to 30° respectively. Once C_s , α_{r1} , and α_{r2} were determined, the feedrate was selected according to equation (1). The choice of the width of chamfer, the value of the negative radial angle and the value of the nose radius greatly affect the ease of chip flow and the resulting surface roughness of the workpiece.

The edge of the negative radial angle lightly contacts with the workpiece and participates in the cutting action. A basic force model of three dimensional milling process, which

can accurately predict the formation of shear planes for the case of face milling with a chamfered main cutting edge, must have not only nose radius R , cutting depth d , feed rate f , cutting speed V , the first radial angle α_{r1} , the second radial angle α_{r2} , and axis direction angle α_a as shown in Table 1.

However, chamfered main cutting tools effects were not included in glass-fiber-reinforced plastics (GFRP) milling. The study was established in order to understand the behavior of GFRP during machining operations. Notably, the shear plane areas must be varied due to the effects of the tool geometry in the cutting process. This work presents some experimental results to clarify details of the GFRP in milling, where several trials were carried out for different tool geometries.

Based on the experimental results of Hoshi [11] and Chang [14], the milling tool geometries were selected then the tool holders were designed and manufactured. The basic model for a sharp corner tool with a chamfered main cutting edge tool ($R=0$) was shown in Fig. 1. Because of the effects of size, shape and tool angle, modified cutting forces is present in this section in order to get the accurate results. As metal is cut under a three dimensional cutting operation, the total energy consumed per units is

$$U = F \cdot V, \quad U = U_s + U_f + U_a + U_m \quad (2)$$

where

U_s is shear energy; U_f is friction energy; U_a is surface energy and U_m is momentum energy. From the experimental results presented by Shaw [13], the surface energy U_a and momentum energy U_m are negligible relative to the other two components and hence to a good approximation: $U = U_s + U_f$

Practically all of the energy associated with a cutting operation is assumed in either plastic deformation or friction, and essentially all of this ends up as thermal energy. The cutting model of sharp face milling tools with a chamfered main cutting edge is shown in Fig. 1, in which the plane containing the cutting velocity V , shear velocity V_s and chip velocity V_c are indicated. The effective rake angle(α_e) and effective shear angle(ϕ_e) are defined in this plane, and the cutting process may be interpreted as piling up of orthogonal cuttings with same and but with different undeformed chip thickness along the cutting edge.

Denoting shear velocity on the shear as V_s , we may write the shear energy U_s as

$U_s = F_s \cdot V_s$, where F_s is the shear force on the shear plane.

The frictional energy per unit time U_f on the tool face is similarly given by the equation

$U_f = F_t \cdot V_c$, where F_t is the frictional force on the tool face.

It was assumed that energy was consumed as shear energy on the shear plane and as friction energy on the tool face. The shear energy per unit time (U_s) and the friction energy per unit time (U_f) [20] can be expressed as:

$$U_s = F_s \frac{V \cos \alpha_e}{\cos(\phi_e - \alpha_e)} = \tau_s A \quad (3)$$

and

$$U_f = F_t V_c = f_t \int_0^{B_1} db V_c = \frac{\tau_s \sin \beta \cos \alpha_e Q V}{[\cos(\phi_e + \beta - \alpha_e) \cos(\phi_e - \alpha_e)]} \quad (4)$$

where A is the shear area, Q is the friction area, $\int_0^{B_1} db$ is the integral width of chip flow direction along the tool face (B_1) is the width measured in the direction orthogonal to the chip flow and db is an increment of integration in the direction. According to Bhatnagar et al. [17] assumed the shear force was calculated using the relations developed for metal machining, and Chang and Fuh [19] demonstrated the shear areas in the cutting medium carbon process with a chamfered main cutting sharp and nose radius (R) tool. For convenient calculation, the shear plane must be projected in the plane perpendicular to the speed of cut where an easy operation of calculation and analysis can be made to save the time of calculation, and for defining chip flow angle in this perpendicular section as η_c , we have the relation between η_c and η'_c on the tool face:

$$\eta'_c = \tan^{-1}[(\tan \eta_c - \sin \alpha_{r2} \tan \alpha_a \cdot \cos \alpha_a / \cos \alpha_{r2})] \quad (5)$$

According to this equation, the shear plane can be verified by changing η_c while a small amount values, and

$$\alpha_e = \sin^{-1}(\sin \alpha_{r2} \cdot \cos \alpha_a \cdot \cos \eta_c + \sin \eta_c \cdot \sin \alpha_a) \quad (6)$$

where α_e is the effective rake angle, α_{r2} is the second radial angle, α_a is the axial angle, ϕ_e is the effective shear angle, β is the friction angle, and τ_s is the shear stress, η_c is the chip flow angle which was determined that minimized the total cutting energy U .

The calculation of shear area A and projected area Q fall into one of the following categories depend on the relationship between nose radius, federate and the depth of cut.

1. Sharpness of the tool is such that its radius equals zero ($R=0$, $R<f$)

The calculations of shear area A and projected area Q , is shown in Fig. 1 [14]. The areas of the shear plane A and the projected area Q of the various cases are obtained as follows: The shear area A is equal to $A_1 + A_2 + A_3$, as illustrated in Fig. 1(a).

$$A_1 = \frac{t_3^2}{4 \cos^2 \alpha_{r2}} \left\{ \frac{4 \cos^2 \alpha_e}{\sin^2 \phi_e \cos^2 \eta_c} - \left[1 + \frac{\cos^2 \alpha_e}{\sin^2 \phi_e \cos^2 \eta_c} - \frac{1}{\cos^2 \eta_c} \cdot [\sin^2 \eta_c + (\sin \alpha_e + \cos \alpha_e \cot \phi_e)^2 - 2 \sin \eta_c \sin \alpha_a (\sin \alpha_e + \cos \alpha_e \cot \phi_e)] \right]^2 \right\}^{1/2} \quad (7)$$

$$A_2 = \frac{t_3 (2b / \cos \alpha_a - t_3 \tan \eta_c / \cos \alpha_{r2})}{2 \sin \phi_e \cos \alpha_{r2} \cos \eta_c} \{ \cos^2 \alpha_e - \sin^2 \phi_e [\sin \eta_c - (\sin \alpha_e + \cos \alpha_e \cot \phi_e) \sin \alpha_a]^2 \}^{1/2} \quad (8)$$

$$A_3 = (W_e^2 \cos^2 \alpha_{r1} \tan C_s) / (2 \cos \alpha_a \sin \phi_e) \quad (9)$$

($A_1 + A_2$) is the area of the main chip, A_1 is the area of triangle BCE , A_2 is the area of trapezoid $CEFD$; and A_3 is the triangular area of the secondary chip, $D\bar{Y}J$. The chamfered width, W_e was constrained by the empirical

formula (1).

The area of the projected cross-section Q is equal to $Q_1 + Q_2 + Q_3$, where Q_1 is the area of trapezoid $BCDL$; Q_2 is the area of rectangle $CC' DD'$ and Q_3 is the area of triangle $DD' \bar{Y}$ (Figs. 1a and 2).

$$Q_1 = \frac{1}{2} \left(\frac{b_2 + b}{\cos \alpha_a} \right) \cdot \frac{t_3}{\cos \alpha_{r2}} \quad (10), \quad Q_2 = W_e b_2 / \cos \alpha_a \quad (11)$$

$$Q_3 = (W_e^2 \cos \alpha_{r1} \tan C_s) / (2 \cos \alpha_a) \quad (12)$$

2. Nose radius of the tool (R) is smaller than the federate (f), $R \neq 0$, $R < f$, as shown in Fig. 2.

The shear area A includes here both the area of (1) and the cylindrical area formed by the tool nose radius [19].

3. Nose radius of the tool (R) is larger than the federate (f), $R \neq 0$, $R > f$

According to the depth of cutting, which can be subdivided into three parts: (a) $d > R$, (b) $d = R$, and (c) $d < R$, as shown in Fig. 3 [19]. Although paper focuses on cases with a sharpness of the tool, such as in case (2) and (3), a further simulation is under wait to study the case of large nose radius cutting, and the results will be reported in the future.

Expressions for $t_1, t_2, t_3, f_1, b, b_2$ and b_4 are shown in Appendix; b is the width of cut. It was assumed that energy was consumed as shear energy on the shear plane and as friction energy on the tool face.

According to Wang [16], the normal and shear forces along the fiber direction were calculated to assume that the measured resultant force equivalent to that present in the workpiece at the tool point. Transformation equations used to obtain the normal and shear forces (N_s, F_s) along the fiber direction in terms of the principal and thrust (F_c, F_t) components are shown in Eqs. (13) and (14) [16].

$$N_s = F_c \sin \theta + F_t \cos \theta \quad (13), \quad F_s = F_c \cos \theta - F_t \sin \theta \quad (14)$$

where θ denotes the angle between the fiber orientation and the trim plane. The shear force F_s was calculated using the relations developed for metal machining [16].

Bhatnagar et al. [17] showed that while the classical Merchant's model [21] is applicable to homogeneous materials and their alloys. He applies this model in the machining of FRP in the $-\theta$ cutting direction as a first approximation. He assumes the shear plane angle as the fiber angle where failure occurs. By substituting θ for ϕ in Merchant's model, a basic relationship for the two components of the cutting force with the geometry of the cutting can be obtained from Eqs. (16) and (17) [17].

$$\phi = 45 - \beta/2 + \alpha/2 \quad [21] \quad (\alpha \text{ is the back rake angle}) \quad (15)$$

$$F_c = t_o A_o \frac{\cos(\beta - r)}{\sin \theta \cos(\theta + \beta - r)} \quad (16),$$

$$F_t = \tau_o A_o \frac{\cos(\beta - r)}{\sin \theta \cos(\theta + \beta - r)} \quad (17)$$

$$\tau_s = \tau_{composite} = \tau_{fiber} V_f \quad (V_f \text{ is fiber contains}) [22] \quad (18)$$

where A_o is the area of undeformed chip, β is the mean friction angle, r is the back rake angle, F_c is the main cutting (horizontal) force and F_t is the thrust (transversal) cutting

force. By knowing the shear area A_o of the undeformed chip, the shear strength τ_o was calculated [17], τ_s is the shear stress [22, 23].

The cutting power is a function of at least $\alpha_a, \alpha_{r1}, \alpha_{r2}, d, W_e, C_s, C_e, f, V, \theta_{ref}, \theta, \tau_s, \beta$ and η_c . Assuming that the chip flows up the tool in a direction would minimize the total cutting power U , then by changing η_c was determined to minimize U , for $\alpha_a, \alpha_{r1}, \alpha_{r2}, d, W_e, C_s, C_e, f, V, \theta_{ref}, \theta, \tau_s$ and β were given in the tool specifications and cutting conditions. Once η_c had been determined, then α_e that describe the chip formation could be determined.

The value of η_c for the total minimum power U_{min} to be used in equation (19) was obtained by calculating U for a range of values η_c according to the computer flow chart (Fig. 4). Therefore $(F_H)_{Umin}$ was determined by solving equation (20) in conjunction with the energy method [24].

$U_{min} = V \cdot (F_H)_{Umin}$ and $U_{min} =$ functions of $(\alpha_{r1}, \alpha_{r2}, \alpha_a, d, W_e, \theta_{ref}, C_s, C_e, f, V, \theta, \tau_s, \beta$ and $\eta_c)$ (19)

$$U_{min} = (F_H)_{Umin}, F_H = (F_H)_{Umin} = \frac{U_{min}}{V} = \left\{ \frac{\tau_s \cos \alpha_e A}{\cos(\varphi_e - \alpha_e)} + \frac{\tau_s \sin \beta \cos \alpha_e Q}{\cos(\varphi_e + \beta - \alpha_e) \cos(\varphi_e - \alpha_e)} \right\} \quad (20)$$

where φ_e is the effective shear angle equals to the angle between the fiber orientation angle (θ) and lead angle C_s .

$$F_t = \frac{\tau_s \sin \beta \cos \alpha_e Q}{\cos(\varphi_e + \beta - \alpha_e) \cos(\varphi_e - \alpha_e)} \quad (21)$$

$$N_t = \frac{[(F_H)_{Umin} - (F_t)_{Umin} \cdot \sin \alpha_e]}{(\cos \alpha_{r2} \cdot \cos \alpha_a)} \quad (22)$$

$$F_T = -N_t \cos \alpha_{r2} \sin \alpha_a + F_t (\sin \eta_c \cos \alpha_a - \cos \eta_c \sin \alpha_{r2} \sin \alpha_a) \quad (23)$$

$$F_V = -N_t \cdot \sin \alpha_{r2} + F_t \cos \eta_c \cdot \cos \alpha_{r2}. \quad (24)$$

$$(R_t)_H = N_t \cos \alpha_{r2} \cos \alpha_a + (F_t)_{Umin} \sin \alpha_e = (F_H)_{Umin} \quad (25)$$

$(R_t)_H$ is the horizontal cutting force in the horizontal plane, N_t is the normal force at the tip surface with minimum energy. Because of the effects of size and shape with tool edge wear, a modified cutting force is presented in this paper in order to get more precise results. Besides the $(F_H)_{Umin}$ force, the plowing force F_p due to the effects of the tool specification [19] is considered under the prediction of the horizontal cutting force, as shown in Fig. 5. That is

$$F_{HH} = (F_H)_M + F_p \quad (26), F_p = HB \cdot r_1 \cdot L_f \quad (27)$$

in which r_1 is the radius on the main cutting edge between the face and the flank, and V_b is the length of flank wear. Based on the experimental evidence measuring the length of V_b , the values are between 0.05mm and 0.1mm (cutting time equals 10 min), L_f is the contact length between the cutting edge and the workpiece. L_p is the projected contact length between the tool and workpiece. The contact lengths L_f and L_p are determined for the following conditions (Figs. 6a and 6b), as follows.

$$L_f = \frac{d}{\cos C_s} + \frac{f_1 \cdot \cos C_s}{[\cos(C_e - C_s) \cdot \cos \alpha_{r2}]} = \overline{pm} + \overline{mk} \quad (28)$$

$$L_p = \left(\frac{d}{\cos C_s} \right) \sin C_s + \frac{f_1 \cos C_s \cos C_e}{[\cos \alpha_{r2} \cos(C_s - C_e)]} \quad (29)$$

$$(F_T)_M = F_T + L_p \cdot V_b \cdot \sigma_y \quad (30), (F_V)_M = F_V + L_p \cdot V_b \cdot \tau_y \quad (31)$$

If HB is the Brinell hardness of the workpiece, the expressions of σ_y and τ_y are given by [25]

$$\tau_y = \sigma_y / 2 \quad (32), \sigma_y = HB / \pi \quad (33)$$

Based on Fig. 7, the final modified cutting force F_{HH} components are rewritten for $C_s \neq 0^\circ$ as the following:

$$F_{HH} = (F_H)_M,$$

In Fig. 8 each tooth of the cutter with entry angle and exit angle, are both varied by workpiece and cutter diameter, the values will alter at $\theta_x = 0^\circ \sim 180^\circ$. To understand the whole process of the cutting force pulsation, the complete process ($\theta_i = 0^\circ, \theta_f = 180^\circ$) will be investigated in this paper. Be contrast with the turning operation as shown in Fig. 9(b), the workpiece carries out a rotary motion and the tool has a plane motion. But as long as the feedrate is small, the cutting velocity, the radial angle (α_r), the axial angle (α_a), the undeformed chip thickness, and the normal rake angle, which influence all by less than 5% [26], so that the path can be approximation as a circle without much loss in accuracy. The tooth path of a face milling cutter is a cycloid as shown in Fig. 8. The comparison of tool geometry between the face milling cutter and turning tool is shown in Fig. 9, where the radial angle (α_r), the axial angle (α_a), and lead angle (C_s) of face milling cutter are equal to the second normal side rake angle (α_{s2}), the back rake angle (α_b) and the side cutting edge angle (C_s) respectively. As shown in Fig. 8, the undeformed chip thickness of the tooth path is divided into a series of elements, 10 degrees in each element, in which undeformed chip thickness (t_1) is the central cross section between both side. Comparing the chip cross section with the turning process, we realize that the f (mm/rev) and d of face milling are equal to f (feed per rev) and d (cutting depth) in turning, so that the undeformed chip thickness and cutting width W in face milling process are calculated by the following equations:

$$t_1 = f_\theta \cos C_s \quad (34), f_\theta = f \sin \theta_x \quad W = d / \cos C_s$$

where $f = \text{feedrate} / (\text{rev} \cdot \text{per} \cdot \text{tooth})$.

As shown in Fig. 8, the unit chip cross section and various cutting force components exerted on workpiece at cutting edge are exhibited, in which F_{HH}, F_{VV} and F_{TT} are equal to the cutting force components in turning. Since the directions and magnitudes of the elemental oblique cutting force components F_{HH}, F_{VV} and F_{TT} will vary from element to element, these can be resolved into the fixed and practical directions X (horizontal), Y (transversal) and Z (vertical). Thus the cutting forces are given by

$$F_{TT} = (F_T)_M \cos C_s + (F_V)_M \sin C_s \quad (35)$$

$$F_{VV} = (F_V)_M \cos C_s - (F_T)_M \sin C_s \quad (36)$$

$$F_X = F_{HH} \cos \theta_x + F_{VV} \sin \theta_x \quad (37)$$

$$F_Y = F_{HH} \sin \theta_X - F_{VV} \cos \theta_X \quad (38), \quad F_Z = F_{TT} \quad (39)$$

III. Experimental method and procedure

To verify the proposed force model, experiments were performed and forces were measured with a three-component dynamometer, experimental set-up is shown in Fig. 10. The experiments were on a vertical machining center using a plate face milling process without using any cutting fluids. It was required to measure the cutting force components F_{HH} , F_{VV} and F_{TT} (Figs. 7 and 8) for a range of cutting conditions (cutting speed, feedrate and depth of cut) and tool geometrical factors (radial, axial angle, nose radius, etc.). The machine tool used for the tests was a leadwell vertical machining center (MCV-OP) having a variable feed range with $1 \sim 10000 \text{ mm/min}$, motor with speeds $60 \sim 6000 \text{ rpm}$, rating up to $3.7/5.5 \text{ kW}$. In measuring the cutting forces a Kistler type 9257B, three-component piezoelectric dynamometer was used with a data acquisition system that consisted of Kistler type 5807A charge amplifiers, all measured data were recorded by a data acquisition system (Keithley Metro byte-DAS1600) and analyzed by the control software (Easytest). The reliability of the measurement techniques was checked constantly by repeating the experiments. At the end of each cutting test, the tool flank wear (V_B) was measured using a toolmaker's microscope. Since the manufacturers did not provide tools with selected combinations of lead, radial, axial and inclination angles, special tool holders were designed and manufactured in house are used in the tests. Lead angle (α_a), first and second radial angle (α_{r1} and α_{r2})

To achieve the various cutting geometries, six special cutting tool holders were manufactured to obtain the specified lead angle (C_s) and radial angle (α_r). The cemented carbide tips were ground on a tool grinder. The tool specifications of relief angle, first radial angle (α_{r1}), second radial angle (α_{r2}) and chamfer width are listed in Table 1. The dimensions of these tool holders and tool tips were inspected with a coordinate measuring machine to verify those can meet the specifications. The cutting tool used in the experiment was Sandvik P10 and K10 [27] and the workpieces were GFRP. The workpiece was held in the plain of the dynamometer, and the dynamometer was mounted on the machining center table, and preliminary machining of the workpiece was performed to ensure flatness of the plate. The experimental conditions were maintained the same for all tests, as follows:

1. Dry cutting;
2. Cutting velocity, $V = 285 \text{ m/min}$ ($N = 800 \text{ rpm}$);
3. Cutting depth: $d = 1.0$ and $d = 2.5 \text{ mm}$;
4. Rate of feed: $f = 120 \text{ mm/min}$
($0.15 \text{ mm}/(\text{rev} \cdot \text{per} \cdot \text{tooth})$);
5. The tool holder was vertical to the workpiece;
6. Protrusion of single tool tip from the tool holder was 30 mm .

In the test for each tool geometry the workpiece was

milled 170 mm in the feed direction, while the data were recorded three times at different depths. The results were then averaged. The cutting force, the shapes of chips and tips wear were observed and discussion in section 4.

A. Workpiece

The work material used was 0° ; unidirectional filament wound fiber of E-glass-fiber-reinforced plastics (GFRP) with Vinylester resin composite materials in the form of bars having a square pultruded pipe, size is $50 \times 50 \times 6 \text{ mm}$, and 180 mm length. Table 2 shows some of the physical and mechanical properties of GFRP prior to carry out the cutting experiments [23].

B. Cutting Tools

For achieving cutting geometrical configurations, six cutting tool holders are machined so as to obtain the specified lead angle (C_s), axial angle (α_a), first and second radial angle (α_{r1} and α_{r2}) and also both K and P type carbide tip's which were grounded with a grinder. To have a specified relief angle, negative rake angle and a certain chamfer width, the specifications are listed in Table 1. A total of 6 tool geometries could be made with various combinations of tool holders and tips. The dimensions of these tool holders and tool tips were inspected with a coordinate measuring machine so as to meet the specified requirements.

Two kind of tool materials [27] (Sandvik P10-SIP and K10-HIP) and various tool geometries were employed in the study. Tool compositions of SIP (P type) are listed in the following: WC 56%, TiC 19%, Ta(Nb)C 16% and Co 9.5%; and of HIP (K type) are the following: WC 85.5%, TiC 7.5%, Ta(Nb)C 1% and Co 6%. Oblique milling tests were carried out for each tool. However, for the purpose of comparing tool wear, all cutting tests had a fixed time and the same cutting conditions.

IV. Results and Discussion

From Eqs. (7)-(12), the shear area A and projected area Q were calculated. After the shear area (A) and projected area (Q) were obtained, the shear energy per unit time (U_s) and the friction energy per unit time (U_f) were calculated from Equations (3) and (4). The theoretical principal component of the cutting force, $(F_H)_{U_{\min}}$ was then obtained from Eqs.(19) and (20); the vertical theoretical cutting force (F_V) and the transverse theoretical cutting force (F_T) were obtained from Eqs. (21)-(24). As C_s is not zero, the flank wear and plowing force must be taken into account to obtain the modified three-axis turning forces F_{HH} , F_{VV} and F_{TT} (Fig. 7) that were obtained from Eqs. (25)-(36) and the three axis milling forces F_X (horizontal), F_Y (transverse) and F_Z (vertical) that were obtained from Eqs. (37)- (39) respectively. The values of the theoretical, modified and experimental results for each have F_X , F_Y and F_Z were plotted in Figs. 11-17. The following conclusions were drawn from these results. A series of preliminary tests were conducted to assess the effect of tool material on the tool wear, cutting forces, surface roughness and cutting temperature during the turning of GFRP.

1. The Cutting Forces

According to Chang [14], in Fig. 11, are showed that in face milling of plain carbon steels with chamfered main cutting edge tools decreases about 15% of resultant cutting force, F_R , than unchamfered main cutting edge tool. The increase of the radial angle α_{r1} and α_{r2} , the decrease the total cutting force F_R in case of the constant of lead angle C_s . The increase of the lead angle, C_s , from 20° to 30° is found to induce the decrease of cutting force. However, the cutting force would increase if the angle were increased from 30° to 40° .

The experimental horizontal (F_X), transversal (F_Y) and vertical (F_Z) cutting forces respectively are shown in Figs. 12, 13 and 14 with the sharp P type carbide tool versus C_s of chamfered and unchamfered ($\alpha_{r1} = -30^\circ$, $\alpha_{r2} = 30^\circ$) geometrical configurations. The experimental horizontal (F_X), transversal (F_Y) and vertical (F_Z) cutting forces respectively are plotted in Figs. 15, 16 and 17 with the sharp K type carbide tool versus C_s of chamfered and unchamfered ($\alpha_{r1} = -30^\circ$, $\alpha_{r2} = 30^\circ$) geometrical configurations. The theoretical horizontal (F_X), transversal (F_Y) and vertical (F_Z) cutting forces respectively are shown in Figs. 18, 19 and 20 with the sharp P type carbide tool versus rotation angles and C_s of unchamfered and chamfered ($\alpha_{r1} = -30^\circ$, $\alpha_{r2} = 30^\circ$) geometrical configurations. The theoretical horizontal (F_X), transversal (F_Y) and vertical (F_Z) cutting forces respectively are indicated in Figs. 21, 22 and 23 with the sharp K type carbide tool versus rotation angles and C_s of unchamfered and chamfered ($\alpha_{r1} = -30^\circ$, $\alpha_{r2} = 30^\circ$) geometrical configurations. The results are implied in the following from the above figures:

A. Comparing with milling of carbon steel and GFRP workpiece:

(1) A face milling of GFRP materials with chamfered main cutting edge tools decrease the cutting forces F_X , F_Y and F_Z than unchamfered tool. In Figs. 12 to 17, the results show good agreement with Chang and Fuh in face milling medium carbon steel [14].

(2) In the case of the constant of α_{r1} and α_{r2} , $R=0$., Figs. 12 to 23, the increase of the side cutting edge angle C_s , from 20° to 30° , the cutting forces F_X and F_Y are increased, but C_s from 30° to 40° , the cutting forces F_X and F_Y are decreased, this is different from Fig. 11. Chang [14] studied of milling medium carbon steel, the increase of C_s from 20° to 30° , and the decrease of cutting force. The cutting force would increase if the angle were increased from 30° to 40° . This may be probably for the difference materials, the shear zone is different and during cutting GFRP, the chip is both powder and fiber and the chip was fractured by the tool compressive force loads to fiber. The large C_s , the more fiber chip and the larger the contact between the cutting edge and workpiece will be, and the resistant force F_X and F_Y are produced. As the C_s is more than 30° , the fibers are easier to be cut and the cutting forces F_X and F_Y are decreased. During machining, the cutting zone experiences both thermal and mechanical stresses. This also leads to unstable cutting forces.

B. Comparing with different tool geometries in milling of

GFRP materials

(1) The cutting force values are observed in Figs. 12 to 23, that are the smallest in the case of chamfered tool at $C_s = 20^\circ$,

α_{r1} (α_{r2}) = -10° (10°). The reason is due to decrease the powder chip, and more obvious and smooth formation and flow of the fiber chip are produced. Especially, smaller the C_s , the shorter contact length between the chip and tool, increased the cutting GFRP efficiency and decreased the difficulty of chip formation, as shown in section 4.2, Figs. 24 and 25.

(2) From Figs. 18 to 23, if the plowing force were taken into consideration, the final modified theoretical cutting forces will agree with the experimental values.

C. Comparing with different P and K type of chamfered main cutting edge carbide tools

(1) Due to severe edge chipping, the cutting forces for the chamfered main cutting edge of P type carbide tools were much higher than that experienced by chamfered main cutting edge of K type carbide tools.

2. The shape of chips

Chang and Fuh [14] showed, when face milling of medium carbon steel with chamfered main cutting edge tools, the secondary chip is formed more obviously and has flowed more easily under the situation of $C_s = 30^\circ$, $\alpha_{r1} = -30^\circ$ and $\alpha_{r2} = 30^\circ$. Producing a secondary chip in the case of $C_s = 20^\circ$, $\alpha_{r1} = -10^\circ$ and $\alpha_{r2} = 10^\circ$ is rather difficult.

Knowing the relation between the main chips and secondary chips, the different tool geometrical configurations on various radial angles and lead angles are first attempted to be understood. Nine kinds of tools were used in milling the GFRP workpiece in the same cutting condition. The different chip shapes with P type tool and K type tool are provided in Figs. 24 and 25 respectively.

A. producing a secondary chip in these 6 kinds of chamfered main cutting edge tools is rather difficult and it is formed unobviously.

B. in Fig. (24a), the powder and fiber chip is formed more obviously under the situation of $C_s = 20^\circ$, $\alpha_{r1} = -30^\circ$ and $\alpha_{r2} = 30^\circ$.

C. for producing the powder and fiber chips, in Figs. 24 and 25, the fiber chip is more obviously when the chamfered main cutting edge of P type tool, and the C_s from 20° to 40° , $\alpha_{r1} = -30^\circ$ and $\alpha_{r2} = 30^\circ$ is employed.

D. in milling of GFRP with chamfered main cutting edge tools, no secondary chips are observed for all kind of the tools shown in Figs. 24-25, and the chips are powder and fibers, it is difficult to clarify the shear zone, and the secondary flows unobserved.

3. The wear of tips

A. The chamfered main cutting edge P and K type of milling tool have man grinded according to various designed specifications, however the unchamfered main cutting edge with sharpness milling tool ($R=0$) has the more crater and flank wear than the above tool after milling time about 10 min, as shown in Fig. 27 to 28. The design of chamfered main cutting edge tools are better and more resistance than that of the unchamfered main cutting edge tools.

B. The chamfered main cutting edge tool with the nose radius

($R=0.1$) has the least wear among various tools as observed in Figs. 26, 27 and 28 from a comparison of the wear of the tips. Additionally, the chamfered main cutting edge with sharpness tool ($R=0$) has a medium level of wear, and unchamfered tool ($R=0$) has the largest. The reason is that the formal tools possess a lower oxidation wear associated with low temperature at chamfered main cutting edge and the chip produces more easily and these tools have the smaller cutting forces among the other tools.

C. K type of chamfered main cutting edge carbide tools sustained to the least tool wear compared to P type of chamfered main cutting edge carbide tools. This is undoubtedly due to K type of tools superior hardness and wear resistance, as well as low coefficient of friction together with high thermal conductivity. On the other hand the P type of tools suffered from excessive crater wear and chipping.

4. The surface roughness of the workpiece

The surface roughness of workpiece Ra (μm) vs. nose radius tools R and various C_s at $\alpha_{r1}(\alpha_{r2}) = -30^\circ(30^\circ)$ chamfered and unchamfered main cutting edge P and K type tools is shown in Fig. 29.

A. In Fig. 29, in the case of $C_s = 20^\circ$, at $R=1.0$ with K type of chamfered tool, the values of surface roughness Ra is the smallest.

B. For constant C_s , in Fig. 29, increasing the side rake angle α_{r1} and α_{r2} of P and K type chamfered tool, enhances the surface roughness Ra . The reason is due to increase the fiber chip and less obvious powder chip and larger the cutting force. The increase of C_s is from 20° to 30° , increase of surface roughness. However, the surface roughness would decrease if the angle is increased from 30° to 40° . This would be the C_s more than 30° , the fiber is easier to be cut and the cutting forces are decreased as shown in Figs. 20, 23, 24 and 25. However, the largest Ra occurs while the C_s is 30° of P type chamfered cutting tool.

C. In Fig. 29, for constant C_s , increasing the nose radius R but decreasing the side rake angle α_{r1} and α_{r2} , reduces the surface roughness Ra of P and K type chamfered and unchamfered tool. The larger the nose radius R, the lower the surface roughness Ra .

V. Conclusions

A series of preliminary tests were conducted to assess the effect of tool geometries of P and K type of chamfered main cutting edge carbide tool on the tool wear, cutting forces, and workpiece surface roughness during the milling of GFRP. Due to the K type of tools superior hardness and wear resistance, as well as low coefficient of friction together with high thermal conductivity, it was shown that chamfered main cutting edge K type carbide tools sustained the least tool wear, compared to unchamfered K and P type of tool. The cutting forces, and workpiece surface roughness for the chamfered main cutting edge of P type carbide tools in milling were much higher than experience by chamfered main cutting of K type carbide tools. On the other hand, the K type of chamfered main cutting carbide tools suffered from lower

crater wear and chipping. K type of chamfered main cutting edge tools with C_s equals 20° , the conditions $f=120mm/min$, $\alpha_{r1} = -20^\circ$, $\alpha_{r2} = 20^\circ$, produce the lower cutting forces and tip wear. Chamfered main cutting edge tools have the advantage of a limited chip contact length within the tool face. If the chamfer width is suitable, the effect not only diminishes the cutting forces and tool wear but also improves the surface roughness of the workpiece. Further work will be extended to the analysis of large nose radius tool in milling GFRP and CFRP materials with chamfered main cutting edge tools. Another important thing about GFRP machining is workshop environment; the powder and fiber chip generated irritates the skin and is dangerous for the health. The use of a vacuum cleaner, and safety protections for the operators are highly recommended.

In all experiments, milling of GFRP, the cutting forces presented small values compared to milling of carbon steel, the small forces values observed could be explained by the fact that the chip generated as the cutting is a powder and fiber, set it does not present tool cutting edge strength. The new tool model is presented which propose a new concept for calculating the variation of shear areas using the energy approach to predict 3-dimensional face milling cutting forces while tool chamfered and unchamfered. A force model has been built to predict the cutting forces of face milling GFRP, either in the case of chamfered or unchamfered sharpness tool ($R=0$). The predicted cutting forces of face milling are in an agreement with those by experiments.

Nomenclature

A :	area of shear plane (mm^2)
C_e :	end cutting edge angle (rad)
C_s :	lead angle(side cutting edge angle) (rad)
d :	depth of cut (mm)
f_θ :	feed rate of cutting position
F_H :	theoretical horizontal cutting force (N)
$(F_H)_M$:	modified F_H (N)
F_{HH} :	final modified $(F_H)_M$ (N)
F_p :	plowing force (N)
F_i :	friction force (N)
F_T :	theoretical transversal cutting force (N)
$(F_T)_M$:	modified F_T (N)
F_{TT} :	final modified $(F_T)_M$ (N)
F_V :	theoretical vertical cutting force (N)
$(F_V)_M$:	modified F_V (N)
F_{VV} :	final modified $(F_V)_M$ (N)
F_X :	milling force in X axis direction
F_Y :	milling force in Y axis direction
F_Z :	milling force in Z axis direction
HB :	Brinell hardness (N/mm^2)
L_f :	length of contact between tool and workpiece (mm)
L_p :	projected length of between tool and workpiece (mm)

N_t : normal force (N)
 Q : projected area of cutting section on tool face (mm^2)
 r_1 : main cutting edge radius (mm)
 R_a : arithmetic average roughness (μ_m)
 t_1 : undeformed chip thickness for each tooth (mm)
 U_f : friction energy per unit time (Nm/s)
 U_s : shear energy (Nm/s)
 V : cutting velocity (m/min)
 V_b : flank wear (mm)
 V_c : chip velocity (m/min)
 V_f : fiber content (%)
 V_s : shear velocity (m/min)
 W_e : chamfering width (mm)
 α_e : effective rake angle (rad)
 α_{r1} : the first radial angle (rad)
 α_{r2} : the second radial angle (rad)
 α_a : axial angle (rad)
 θ_i : entry angle (rad)
 θ_f : exit angle (rad)
 θ_X : alter entry angle (rad)
 θ_{ref} : side relief angle (rad)
 σ_y : yield shear stress (N/mm^2)
 τ_y : yield normal stress (N/mm^2)

Acknowledgement

This work was supported by National Science Council, Taiwan, R.O.C. under grant number NSC 92-2622-E-197-002-CC3

Appendix

Coefficients of the tool having a sharp corner ($R=0$) without tool wear

$$t_1 = f \cos C_s \quad (A1); \quad t_2 = W_e \cos \alpha_{r1} \quad (A2); \quad t_3 = t_1 - t_2 \quad (A3)$$

$$f_1 = f - W_e \cos \alpha_{r1} \quad (A4), \quad b = d / \cos C_s \quad (A5),$$

$$b_4 = t_2 \tan C_s \quad (A6), \quad b_2 = b - b_4 \quad (A7)$$

References

- [1] S.K. Malhotra, "Some studies on drilling of fibrous composites," *Journal of Materials Processing Technology*, 24, 1990, pp. 292-300.
- [2] H. Hocheng, H.Y. Tsai, J. J. Shiue, and B. Wang, "Feasibility study of Abrasive-Waterjet Milling of Fiber-reinforced plastics," *J. of Manufacturing Science and Engineering, ASME*, vol. 119, 1997, pp.133-142
- [3] K. S. Kim, D.G. Lee, Y. K. Kwak and S. Namgung, "Machinability carbon-fiber-epoxy composite materials in turning," *J. of Materials Processing Technology*, vol. 32, 1992, pp. 553-570.
- [4] W. Konig, C.H. Wulf, P. Grass, and H. Willerscheid, "Machining of fiber reinforced plastics," *Ann CIRP*, vol. 34(2), 1985, pp. 537-548
- [5] H.Y. Puw and H. Hocheng, "Machinability test of carbon fiber-reinforced plastics in milling," *J. of Materials and manufacturing*, 1993, pp. 717-729.
- [6] W.A. Kline and R.E. DeVor, "The effect of runout on cutting geometry and forces in end milling," *Int. J. Mach. Tools Desi. Res.*, vol. 23, No. 2/3, 1983 pp.123-140
- [7] K.S. Kim, D.G. Lee and Y.K. Kwak, "Cutting (milling) characteristic's of carbon fiber/epoxy composites," *Trans. of Korean Soc. Mechanical Engineering*, vol. 14(1), 1990, pp. 237-240.
- [8] G. Linbin, *Handbook of composites*, Van Nostrand Reinhold, New York, 1982, pp. 625-629.
- [9] M. E. Gallab, and M. Sklad, "Machining of Al/SiC particulate metal-matrix composites, part I: Tool performance," *J. of Materials Processing Technology*, vol. 83, , 1998, pp.151-158.
- [10] H. S. Kim and K. F. Ehmann, A cutting force model for face milling operations, *Int. J. Mach. Tool Des., Res.*, vol. 33, 1993, pp. 651-673.
- [11] K. Hoshi and T. Hoshi, "Silver-white chip (SWC) cutting tools", in: *metal cutting technology*, Kogyo Chosakai Publishing, Japan, 1969, pp. 87-104.
- [12] T. Hoshi, "Recent development in silver white chip cutting in: proceeding of the international conference on cutting tool materials, Fort Mitchell, KY. USA, 1980, pp. 15-17.
- [13] M. C. Shaw, "Tool materials, in metal cutting principles", Oxford Press, USA, 1984, pp. 335-367
- [14] C.S. Chang, "A study of high efficiency face milling tools", *J. of Materials Processing Technology*, vol. 100, 2000, pp. 319-340.
- [15] P.S. Sreejith, R. Krishnamurthy, S.K. Malhotra and K. Narayanasamy, "Evaluation of PCD tool performance during machining of carbon/phenolic ablative composites", *J. of Materials processing Technology*, vol. 104, 2000, pp. 53-58.
- [16] D.H. Wang, M. Ramulu and D. Arola, "Orthogonal cutting mechanisms of Graphite/Epoxy composite. Part1: unidirectional laminate", *Int., J. of Machine Tools & Manufacture, Design, Research and Application*, vol. 35(12), 1995, pp. 1623-1638.
- [17] N. Bhatnagar, N. Ramakrishnan, N.K. Naik and R. Komanduri, "On the machining of fiber reinforced plastic (FRP) composite Laminates", *Int. J. Machine Tool and manufacture, Research, Design and application*, vol. 35, No.5, 1995, pp. 701-716.
- [18] E. Shamoto and Y. Altintas, Prediction of shear angle in oblique cutting with maximum shear stress and minimum energy principles, *Trans., ASME, J. of Manufacturing Science and Engineering*, vol. 121, 1999, pp. 399-407.
- [19] K.H. Fuh and C.S. Chang, "Prediction of the cutting forces for chamfered main cutting edge tools", *Int. J. of Machine Tools & Manufacturing Desi., Rese., and Appli.*, vol. 35(1), 1995, pp. 1559-1586.
- [20] E. Usui, A. Hirota and M. Masuko, "Analytical prediction of three-dimensional cutting process. Part 1:Basic cutting model and energy approach," *trans. ASME* 100, 1978, pp. 222-228.
- [21] M. E. Merchant, "Basic mechanics of the metal cutting

process," J. of Applied Mechanics, Trans of ASME, vol. 66, , 1944, pp. 267.

[22] B.W. Rosen and N.F. Dow," Overview of composite materials, Analysis and Design", in Engineered Materials handbook, vol. 1, (Metals park, OH: American Society for Metals, 1987, pp. 175-180.

[23] C.C. Liu,"FRP and GTI Composites", Golden Talent Industries Co. Ltd., Fu-Kou, Hsin-Chu, Taiwan, R.O.C. 2002.

[24] G.V. Reklaitis, A. Ravindran and K.M. Ragsdell, "Region-Elimin. Method, Engineering Optima. Methods and Application", Willy-Interscience Press, New York, 1984, pp. 37-38.

[25] N.H. Cooks,"The mechanics of chip formation, in manufacturing analysis", published by Addison-Wesley, Co. Inc., MA, 1969, pp. 37-38.

[26] H.T. Young, Application of predictive of machining theory to more complicated processes including single-point oblique cutting tools with other than single straight cutting edges and milling and experimental verification, Ph. D., Universities of New Wales, Australia, 1986.

[27] K. J. A. Brookes, World Directory and Handbook of Hard metals, 5th edition, published by International carbide data handbook, United Kingdom, pp. D172-175, 1992.

Received **

** ,2004

Accepted **

** ,2004

Table 1 Tool geometrical specifications

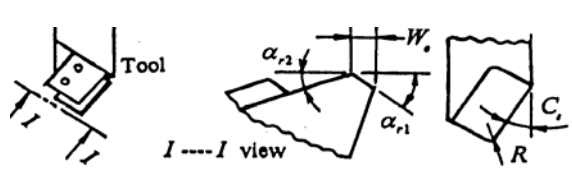
lead angle, C_s	tool No	radial angle (α_{r1}, α_{r2})	nose radius (R), unit: mm 	carbide tool
20°	1	-20°, 20°	sharp(R=0), chamfered(R=0, R=.3, R=.5, R=1.0)	P10, K10
20°	2	-30°, 30°	sharp(R=0), chamfered(R=0, R=.3, R=.5, R=1.0)	P10, K10
30°	3	-20°, 20°	sharp(R=0), chamfered(R=0, R=.3, R=.5, R=1.0)	P10, K10
30°	4	-30°, 30°	sharp(R=0), chamfered(R=0, R=.3, R=.5, R=1.0)	P10, K10
40°	5	-20°, 20°	sharp(R=0), chamfered(R=0, R=.3, R=.5, R=1.0)	P10, K10
40°	6	-30°, 30°	sharp(R=0), chamfered(R=0, R=.3, R=.5, R=1.0)	P10, K10

Table 2 Properties of the work materials GFRP [23]

nominal form	density gm/cm^3	thermal conductivity $kCal/hr\ ^\circ C$	fiber contain	coefficient of thermal expansion ($10^{-6}/^\circ C$)	thermo-setting resins	hardness (Shore, Hs)	tensile strength (kg/mm^2)	compressive strength (kg/mm^2)	modulus tensile (kg/mm^2)	shear strength (kg/mm^2)
roving continuous strand	1.7~2.0	0.21~0.28	72%	2~9	Unsaturated-polyester Resin(Isophthalic)	55~60	30~50	30~50	1500~3000	18

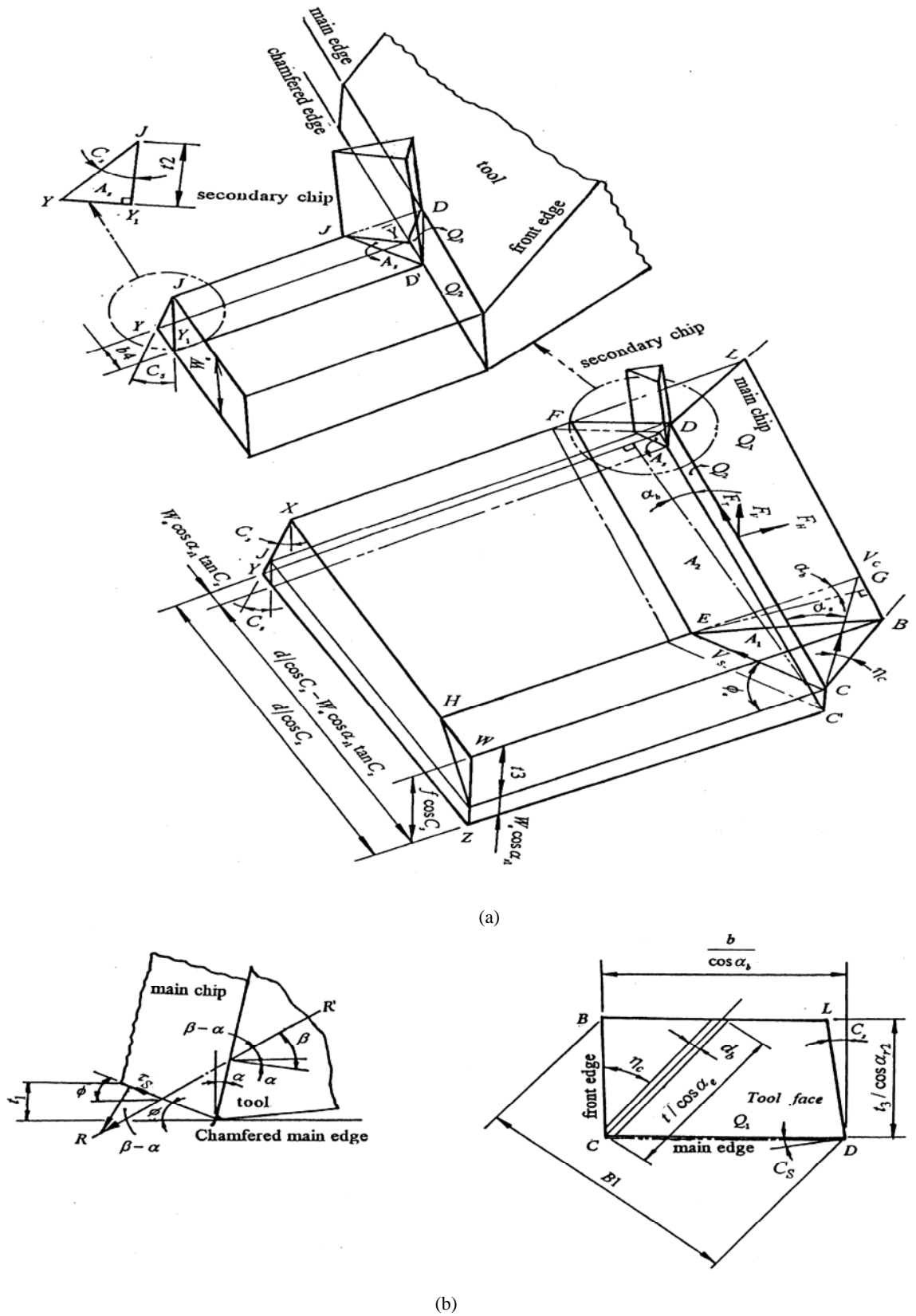


Fig. 1 (a) (b) Basic model of the chamfered main cutting edge tool, $f > R$, $R = 0$ ($\alpha_{s1} = \alpha_{r1}$)

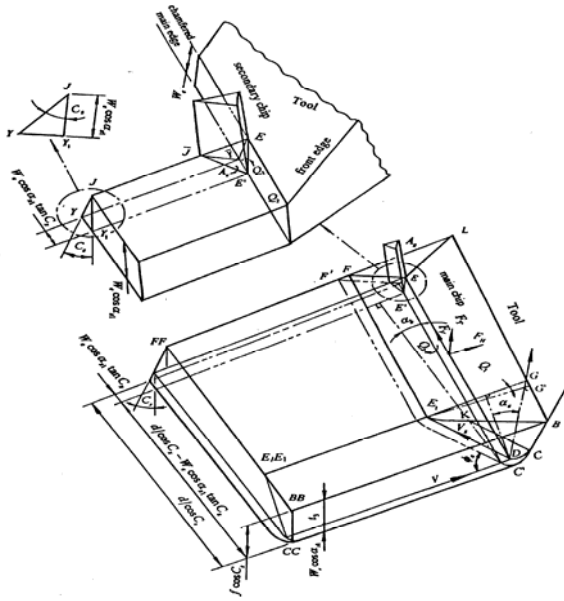


Fig. 2 Basic model of the chamfered main cutting edge tool, $f > R, R \neq 0$

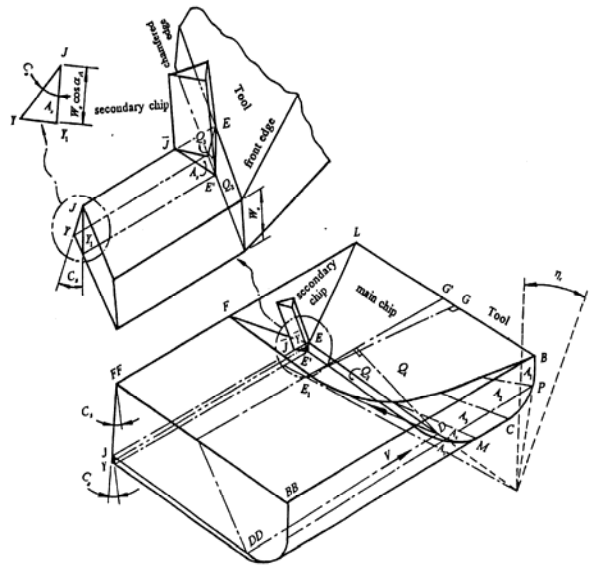


Fig. 3 Basic model of the chamfered main edge tool $f < R, R \neq 0$

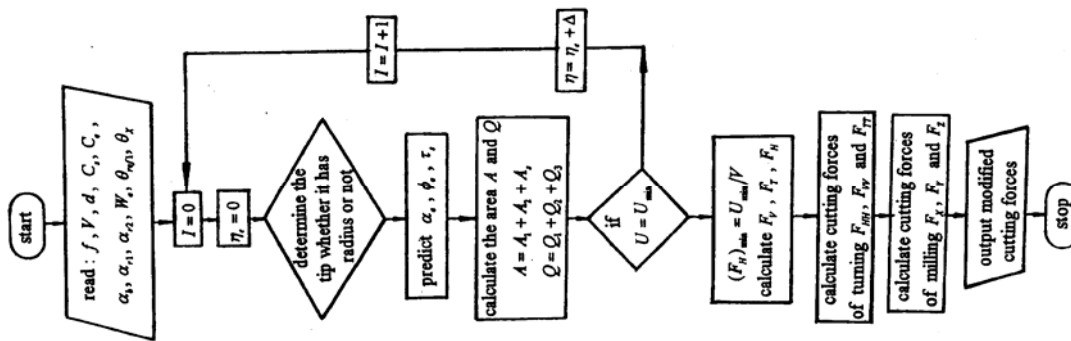


Fig. 4 The flow chart of cutting force prediction

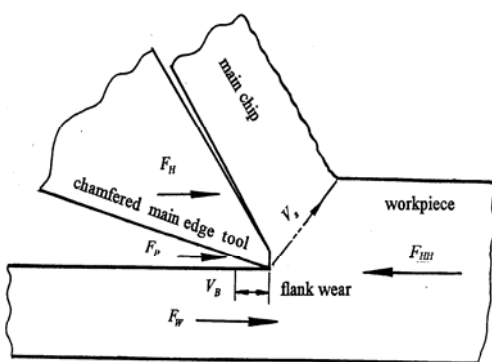


Fig. 5 Horizontal cutting force of F_{HH}

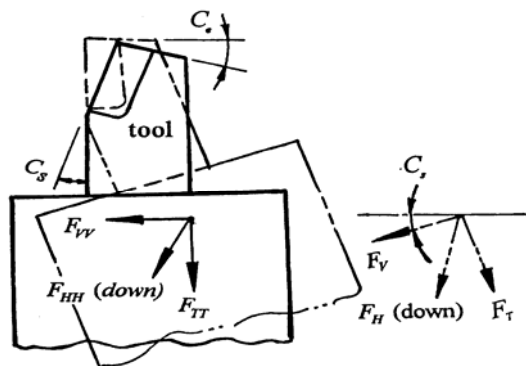


Fig. 7 Final modified cutting force for $C_s \neq 0^\circ$

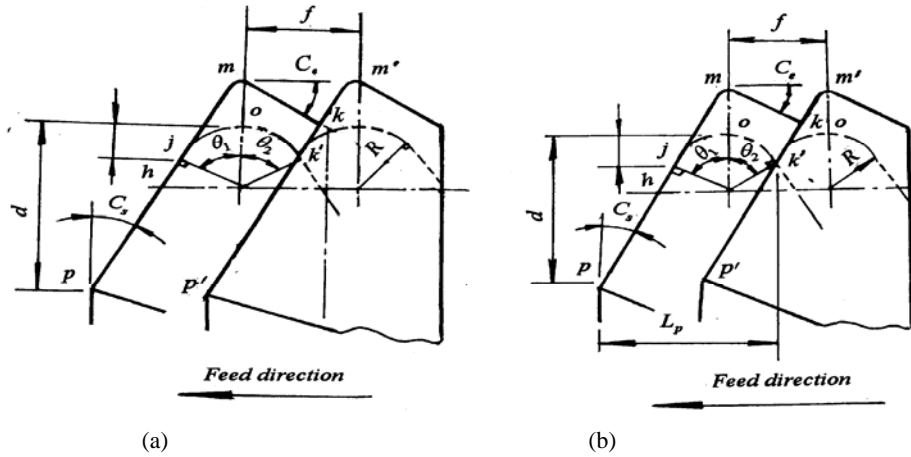


Fig. 6 Figures for calculation of the contact length (a) L_f ($L_f = \overline{pm} + \overline{mk}$) and (b) L_p (projection length) between the cutting edge tool and the workpiece

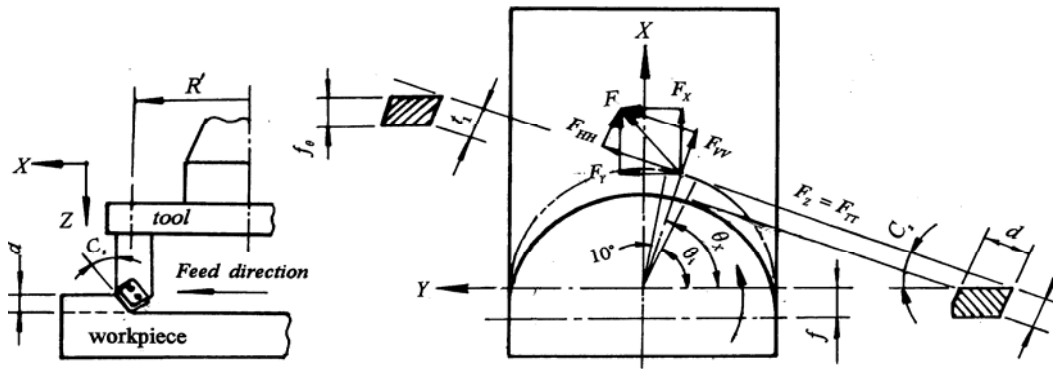


Fig. 8 cutting forces model with face milling and cutting geometric relationship

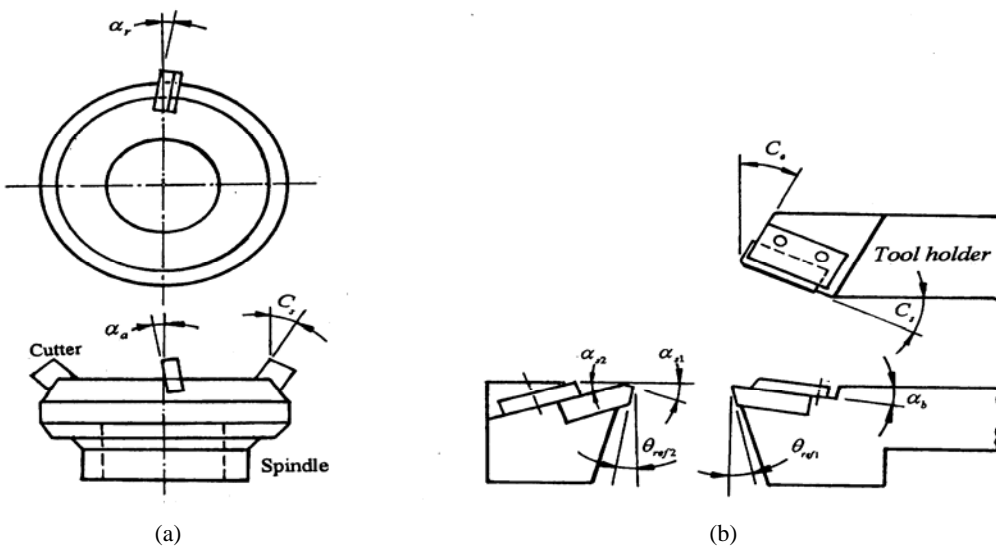


Fig. 9 The tool geometrical angles for (a) a milling cutter, and (b) a turning tool

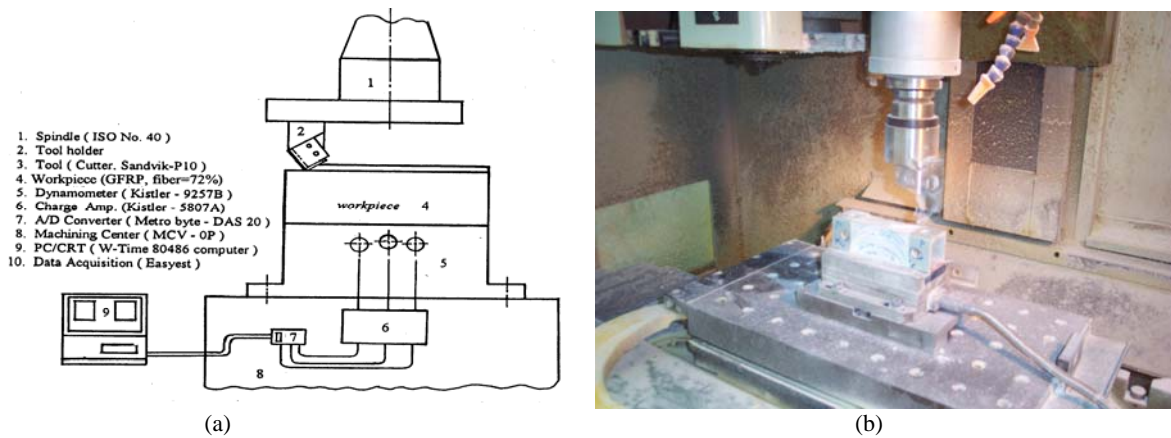


Fig. 10 The experimental set-up (a) machining center and dynamometer, (b) tool and GFRP workpiece

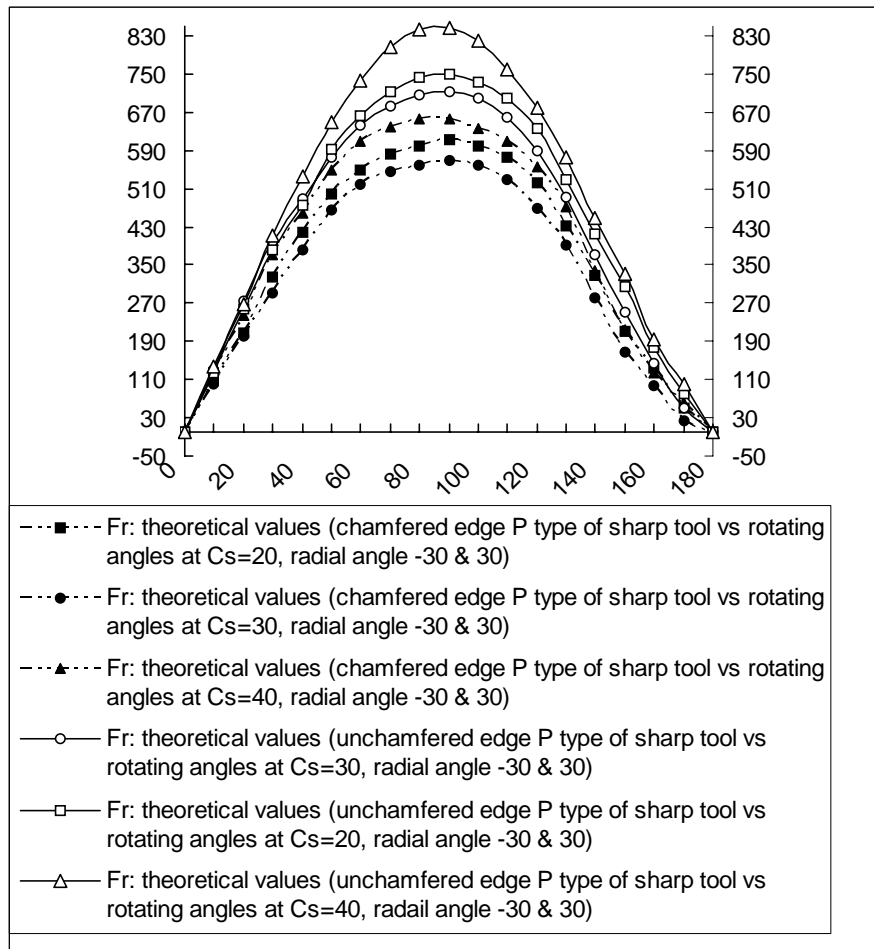


Fig. 11 The resultant theoretical cutting forces: Fr (N) vs. C_s and rotation angles, θ_x for a chamfered and unchamfered tools $\alpha_{r1} = -30^\circ$ and $\alpha_{r2} = 30^\circ$ at $d=1$, $f=45\text{mm/min}$ and $V=75\text{m/min}$ (medium carbon steel) respectively

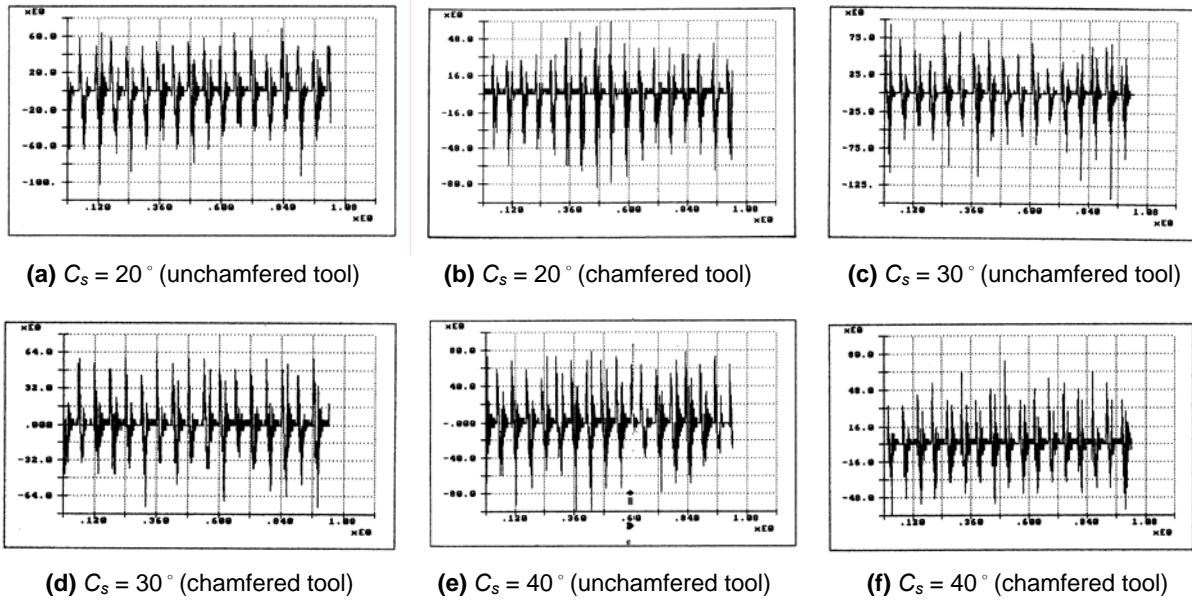


Fig. 12 Experimental horizontal cutting forces F_x (N) vs. C_s of chamfered and unchamfered P type carbide tools at α_{r1} (-30°) and α_{r2} (30°), $d=2.5$, $f=120\text{mm}/\text{min}$ and $V=285\text{m}/\text{min}$ (GFRP) respectively

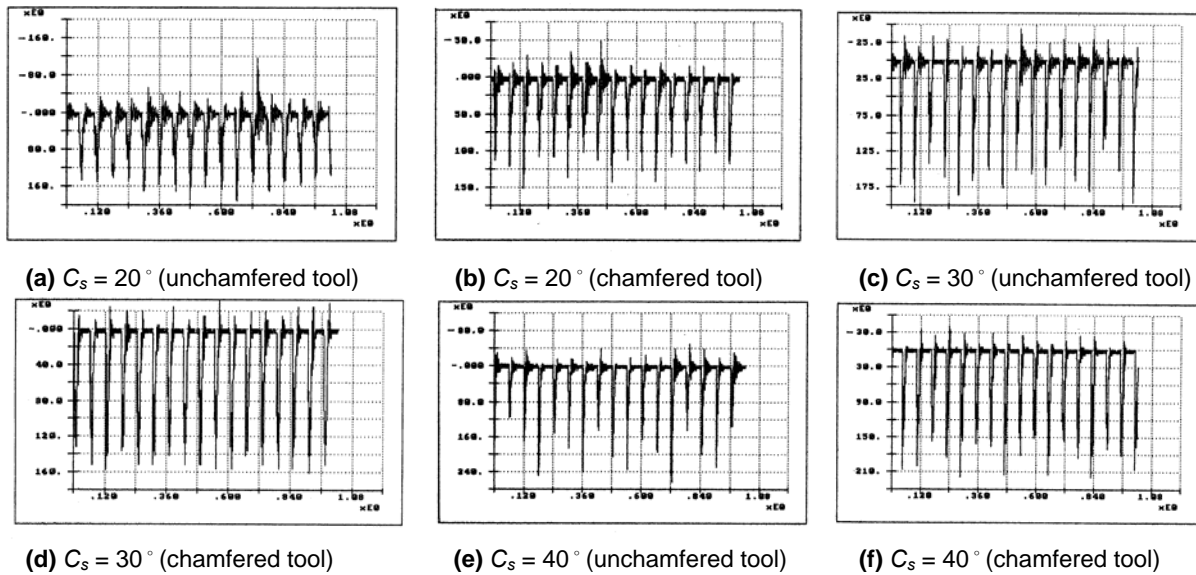
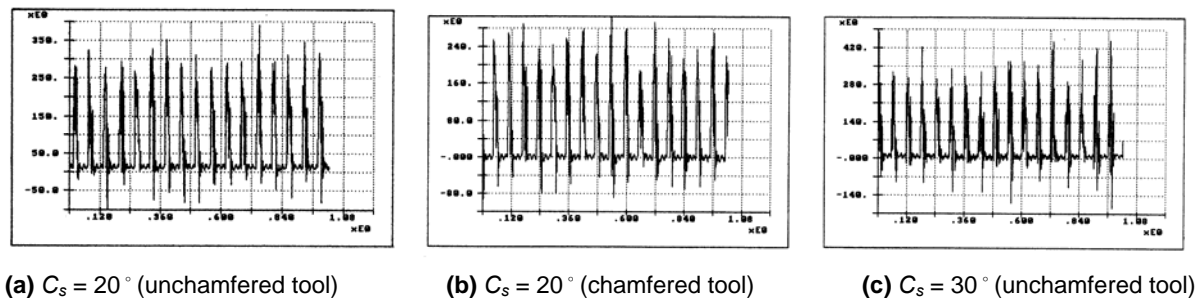


Fig. 13 Experimental transversal cutting forces F_y (N) vs. C_s of chamfered and unchamfered P type carbide tools at α_{r1} (-30°) and α_{r2} (30°), $d=2.5$, $f=120\text{mm}/\text{min}$ and $V=285\text{m}/\text{min}$ (GFRP) respectively



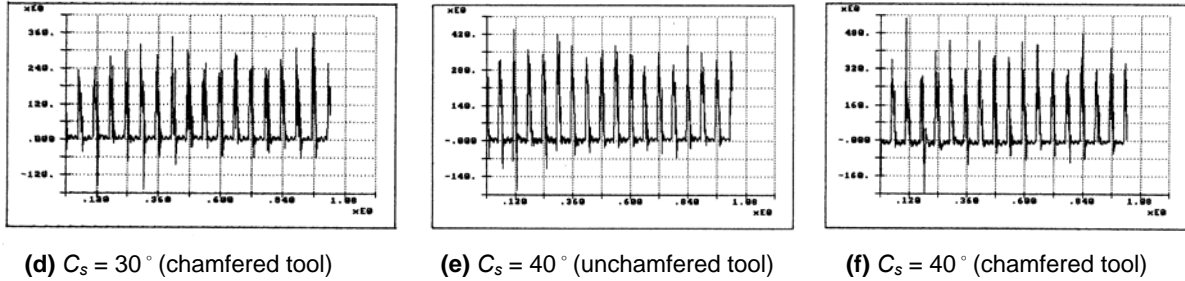


Fig. 14 Experimental vertical cutting forces $F_z(N)$ vs. C_s of chamfered and unchamfered P type carbide tools at $\alpha_{r1}(-30^\circ)$ and $\alpha_{r2}(30^\circ)$, $d=2.5$, $f=120\text{mm}/\text{min}$ and $V=285\text{m}/\text{min}$ (GFRP) respectively

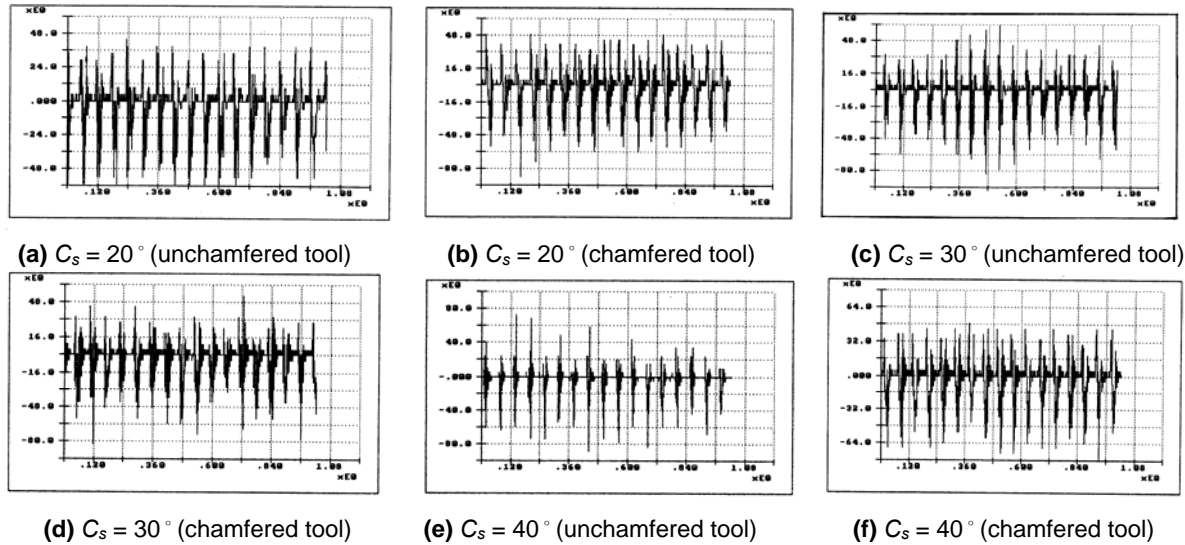


Fig. 15 Experimental horizontal cutting forces $F_x(N)$ vs. C_s of chamfered and unchamfered K type carbide tools at $\alpha_{r1}(-30^\circ)$ and $\alpha_{r2}(30^\circ)$, $d=2.5$, $f=120\text{mm}/\text{min}$ and $V=285\text{m}/\text{min}$ (GFRP) respectively

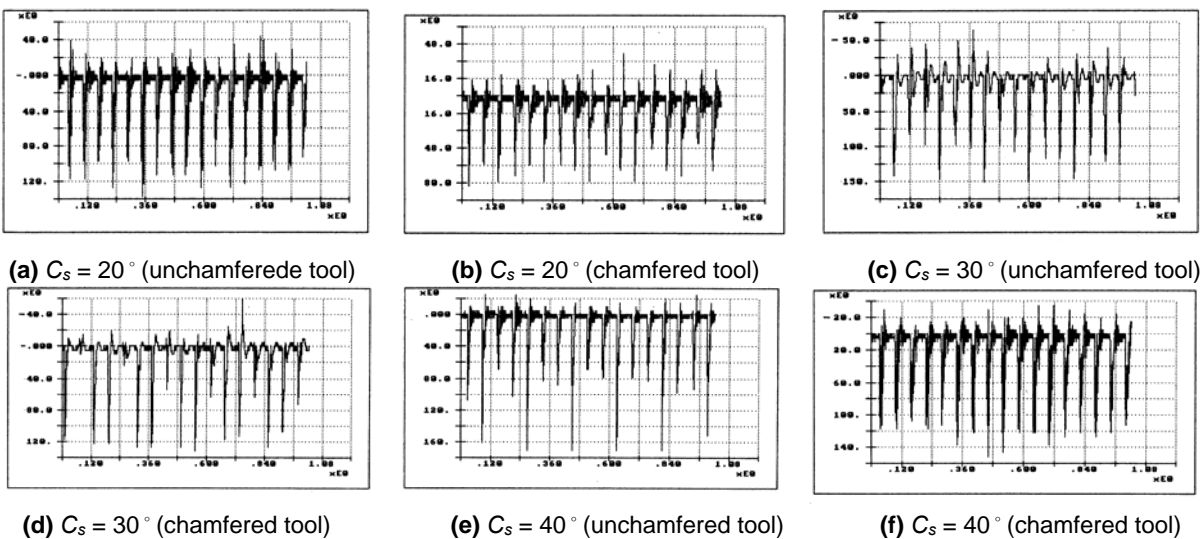
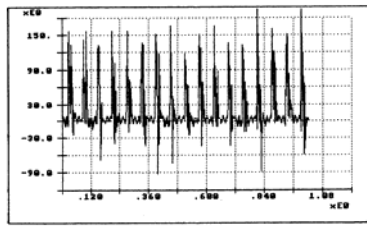
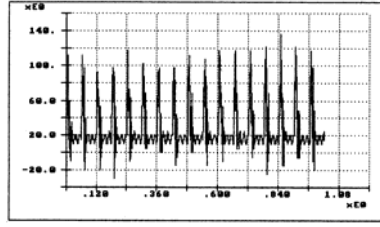


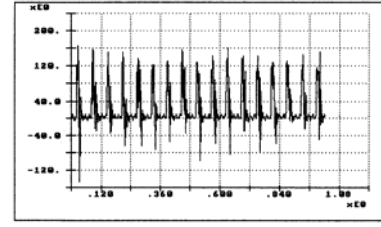
Fig. 16 Experimental transversal cutting forces $F_y(N)$ vs. C_s of chamfered and unchamfered K type carbide tools at $\alpha_{r1}(-30^\circ)$ and $\alpha_{r2}(30^\circ)$, $d=2.5$, $f=120\text{mm}/\text{min}$ and $V=285\text{m}/\text{min}$ (GFRP) respectively



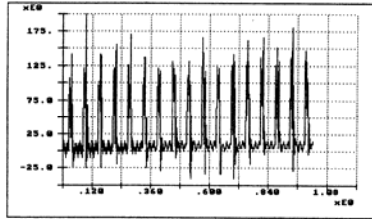
(a) $C_s = 20^\circ$ (unchamfered tool)



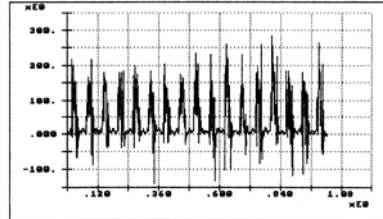
(b) $C_s = 20^\circ$ (chamfered tool)



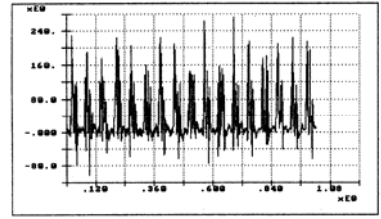
(c) $C_s = 30^\circ$ (unchamfered tool)



(d) $C_s = 30^\circ$ (chamfered tool)



(e) $C_s = 40^\circ$ (unchamfered tool)



(f) $C_s = 40^\circ$ (chamfered tool)

Fig. 17 Experimental vertical cutting forces F_z (N) vs. C_s of chamfered and unchamfered K type carbide tools at α_{r1} (-30°) and α_{r2} (30°), $d=2.5$, $f=120\text{mm}/\text{min}$ and $V=285\text{m}/\text{min}$ (GFRP) respectively

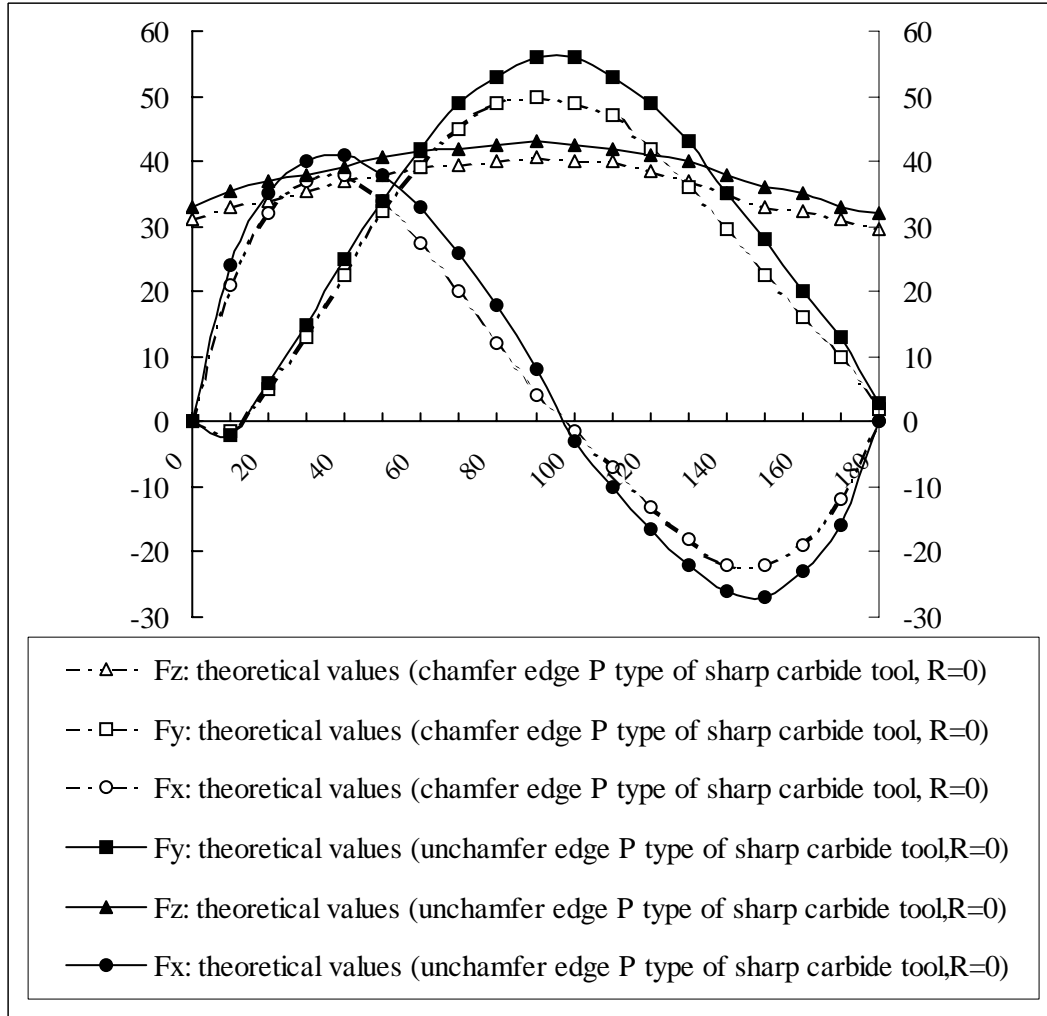


Fig. 18 Theoretical cutting forces : horizontal (F_x), transversal (F_y) and vertical (F_z) vs. rotating angles ($^\circ$) for chamfered and unchamfered main cutting edge P type carbide tool at $C_s=20^\circ$, $\alpha_{r1}(-30^\circ)$ and $\alpha_{r2}(30^\circ)$, $f=120\text{mm}/\text{min}$, $d=2.5$, and $V=285\text{m}/\text{min}$ (GFRP) respectively

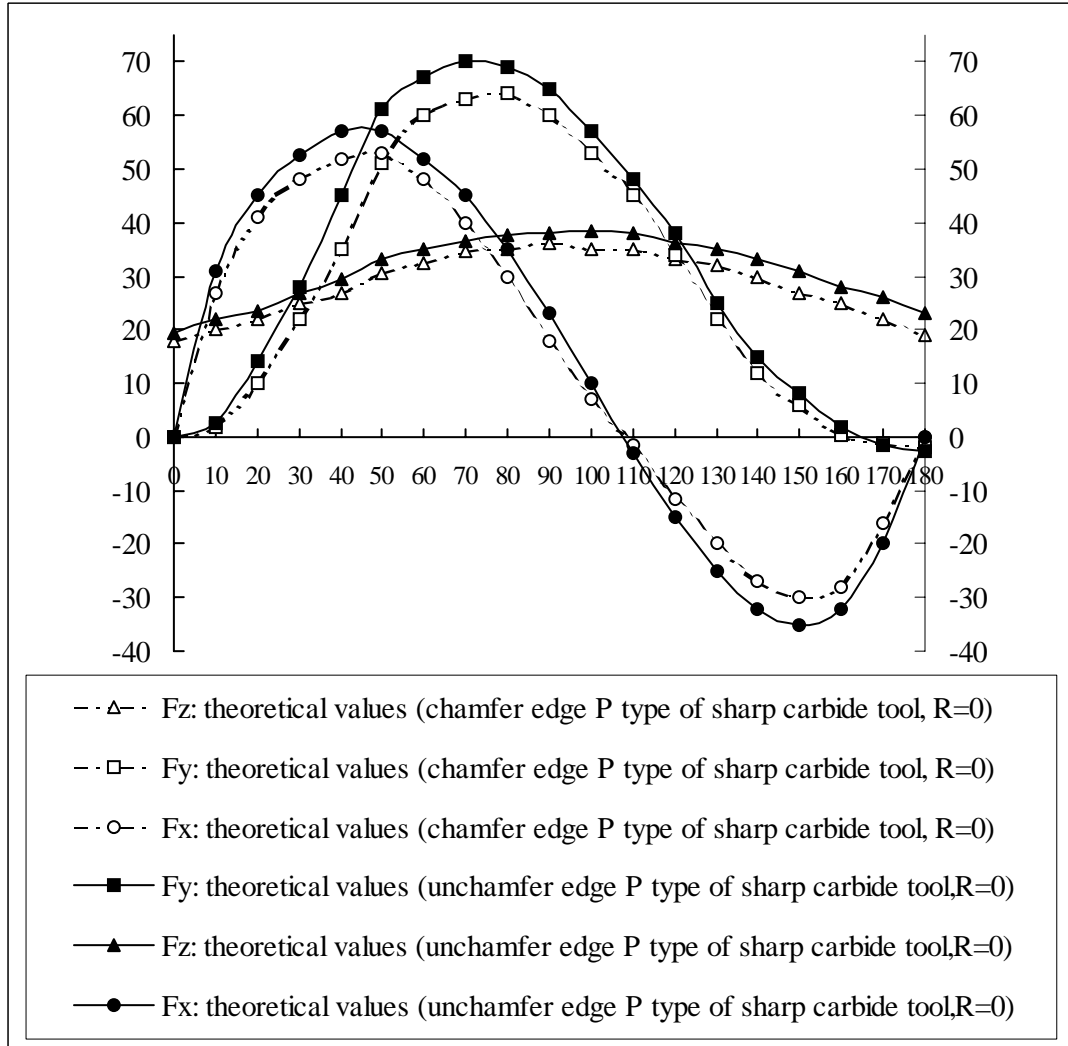


Fig. 19 Theoretical cutting forces : horizontal (F_x), transversal (F_y) and vertical (F_z) vs. rotating angles ($^\circ$) for chamfered and unchamfered main cutting edge P type carbide tool at $C_s=30^\circ$, $\alpha_{r1}(-30^\circ)$ and $\alpha_{r2}(30^\circ)$, $f=120mm/min$, $d=2.5$, and $V=285m/min$ (GFRP) respectively

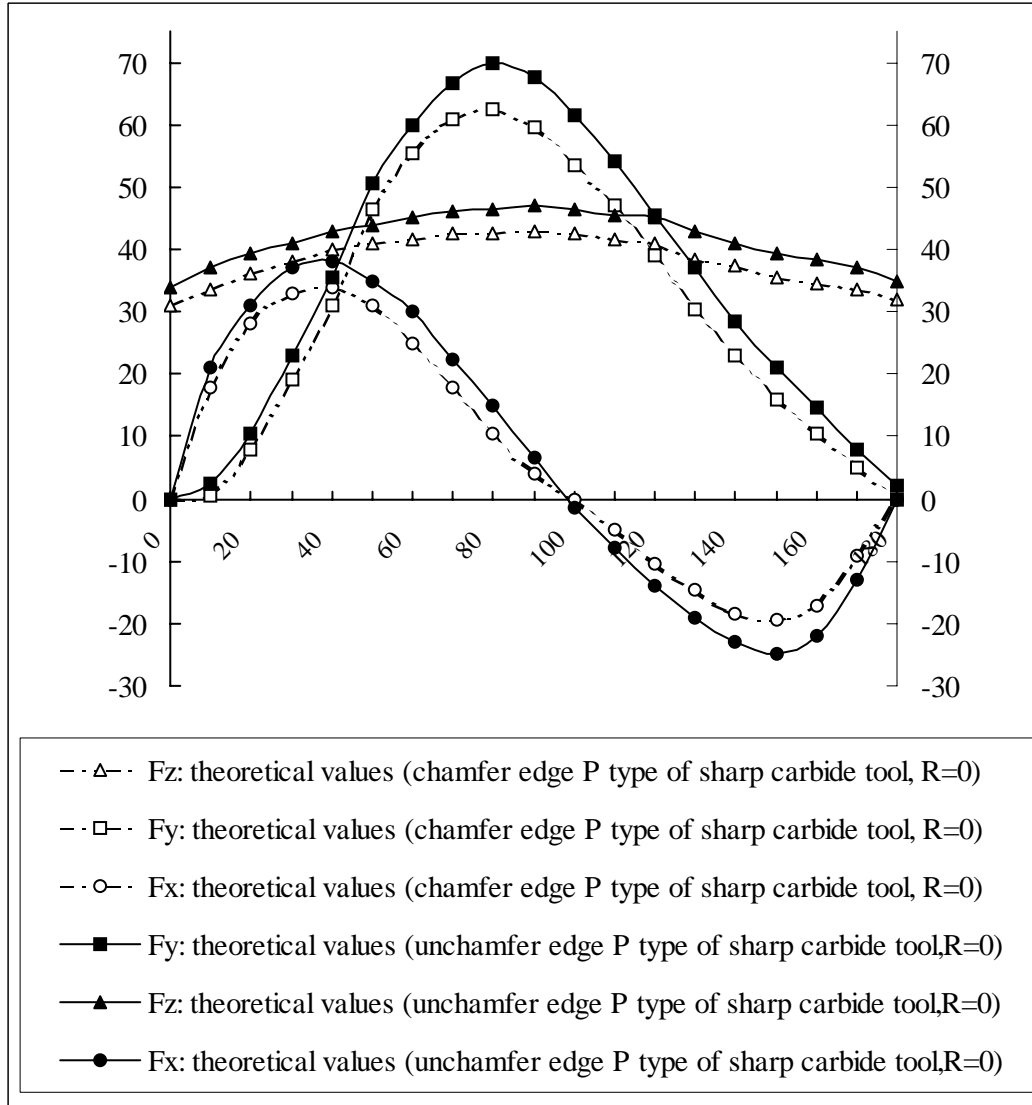


Fig. 20 Theoretical cutting forces : horizontal (F_x), transversal (F_y) and vertical (F_z) vs. rotating angles ($^\circ$) for chamfered and unchamfered main cutting edge P type carbide tool at $C_s=40^\circ$, $\alpha_{r1}(-30^\circ)$ and $\alpha_{r2}(30^\circ)$, $f=120\text{mm}/\text{min}$, $d=2.5$, and $V=285\text{m}/\text{min}$ (GFRP) respectively

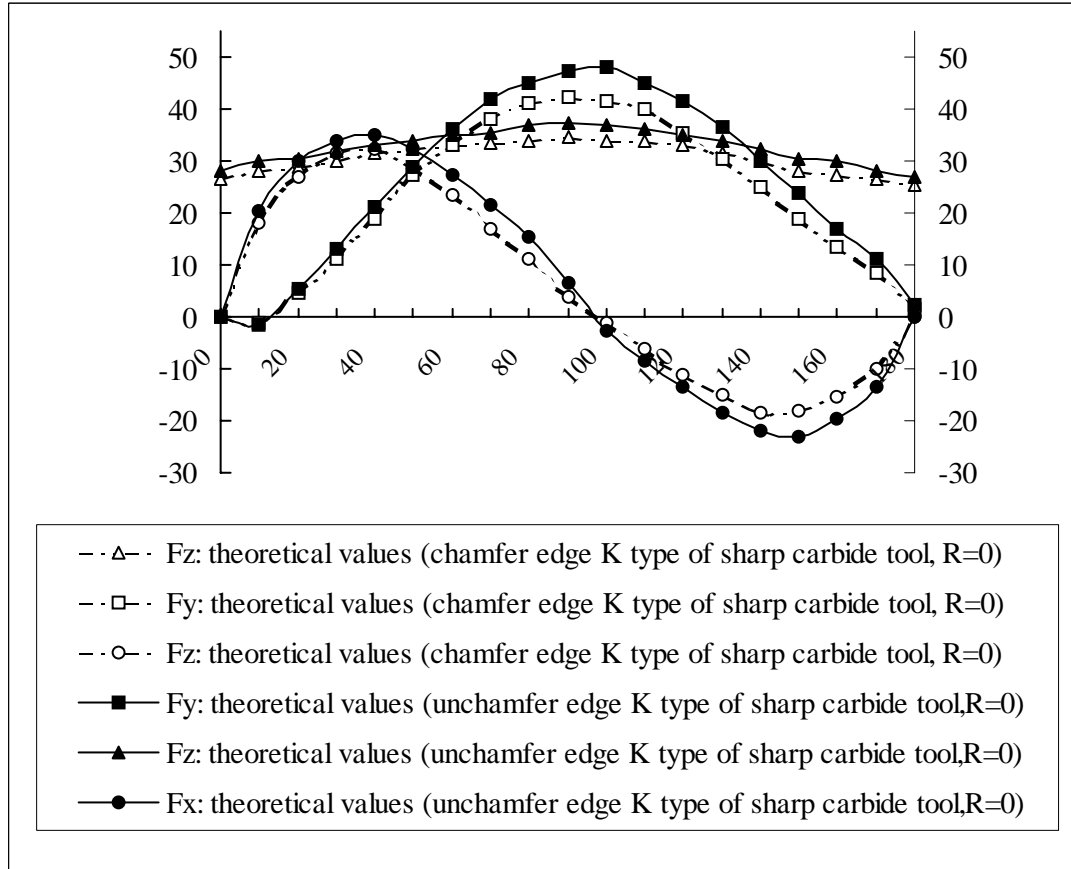


Fig. 21 Theoretical cutting forces : horizontal (F_x), transversal (F_y) and vertical (F_z) vs. rotating angles ($^\circ$) for chamfered and unchamfered main cutting edge K type carbide tool at $C_s=20^\circ$, $\alpha_{r1}(-30^\circ)$ and $\alpha_{r2}(30^\circ)$, $f=120\text{mm}/\text{min}$, $d=2.5$, and $V=285\text{m}/\text{min}$ (GFRP) respectively

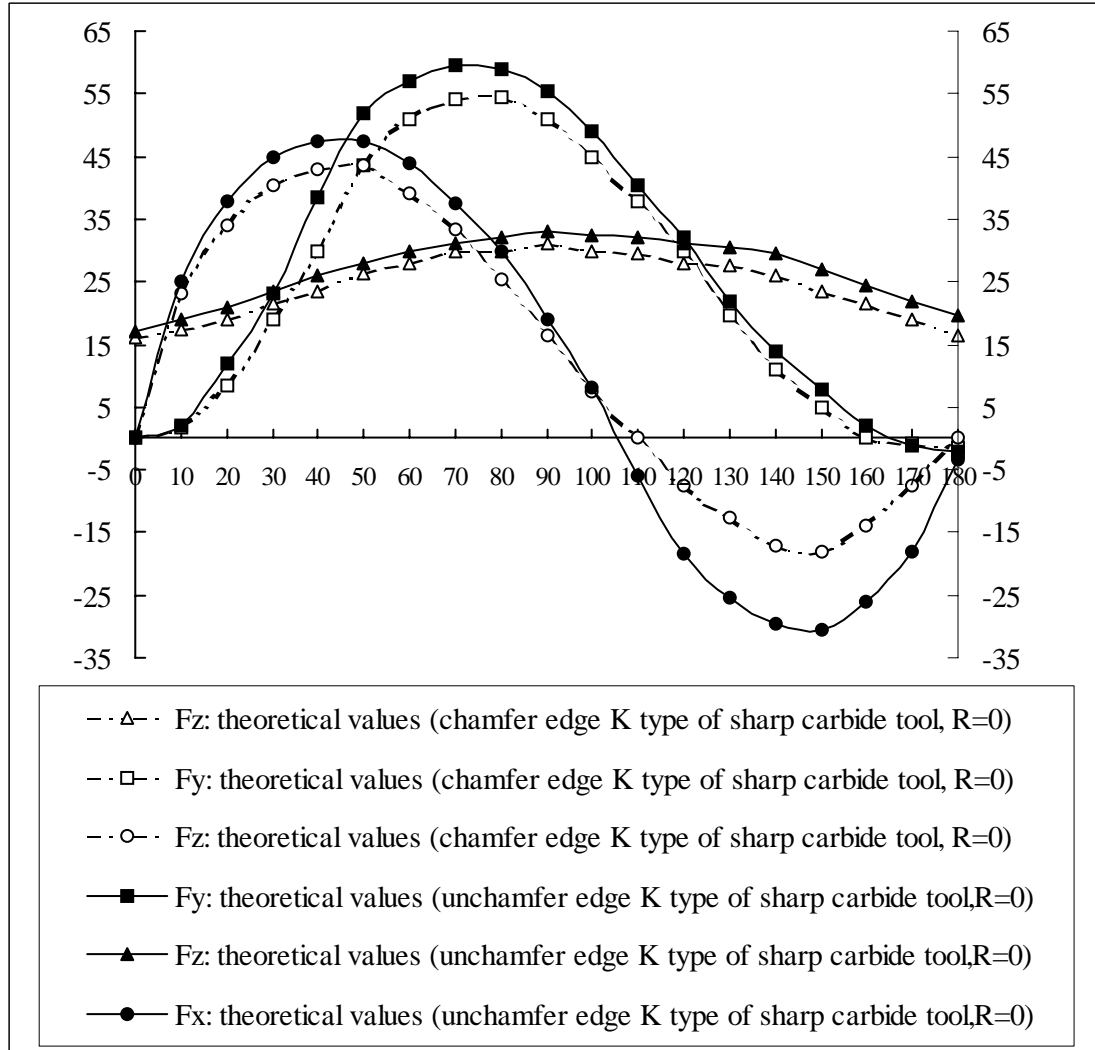


Fig. 22 Theoretical cutting forces : horizontal (F_x), transversal (F_y) and vertical (F_z) vs. rotating angles ($^\circ$) for chamfered and unchamfered main cutting edge K type carbide tool at $C_s=30^\circ$, $\alpha_{r1}(-30^\circ)$ and $\alpha_{r2}(30^\circ)$, $f=120\text{mm}/\text{min}$, $d=2.5$, and $V=285\text{m}/\text{min}$ (GFRP) respectively

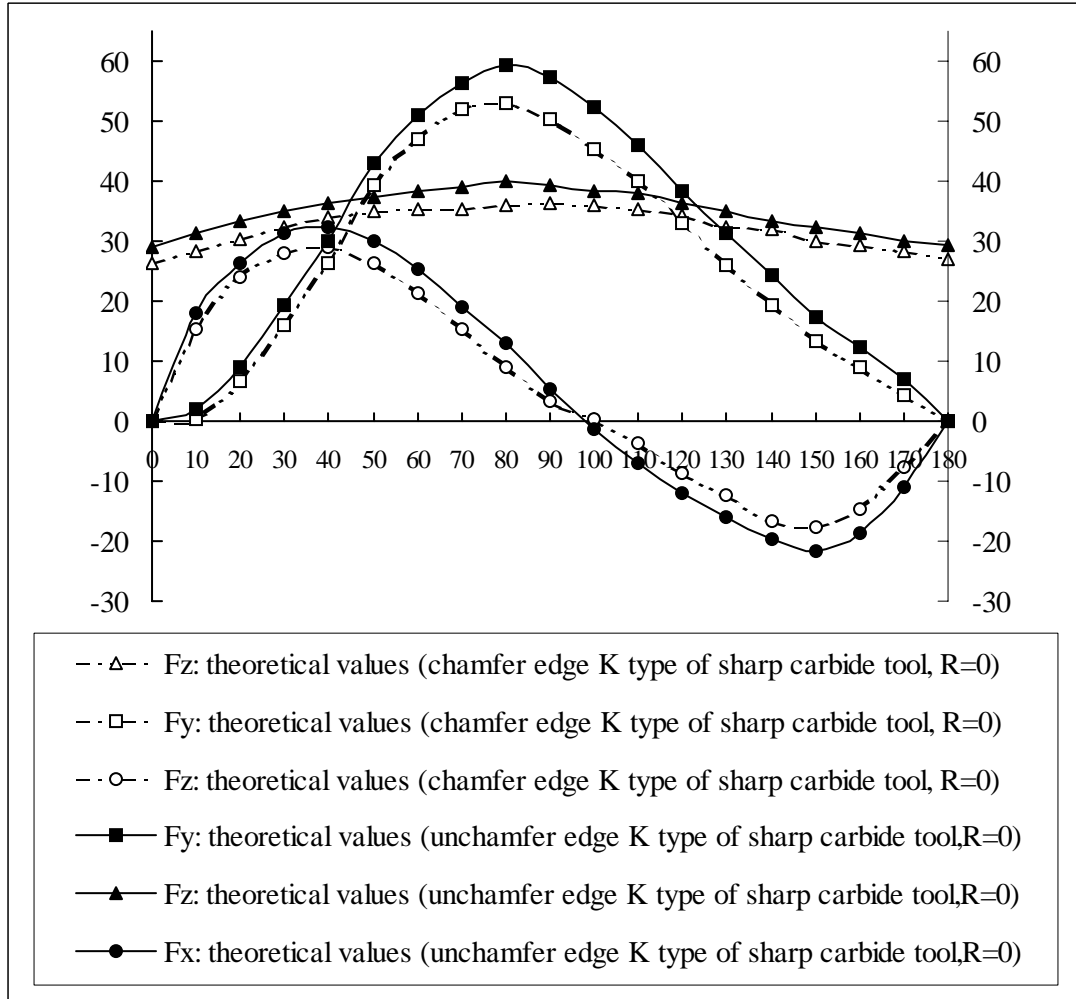
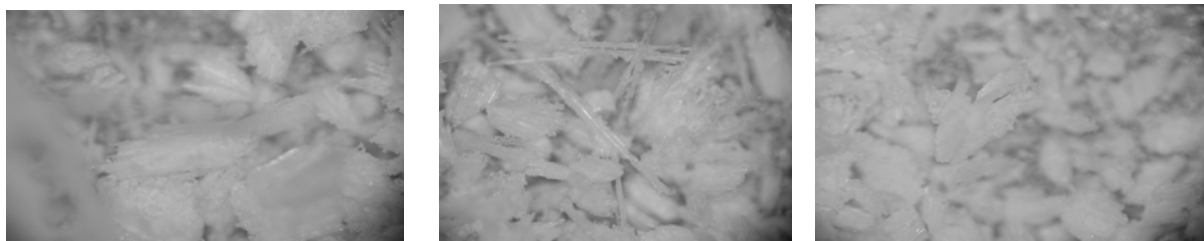
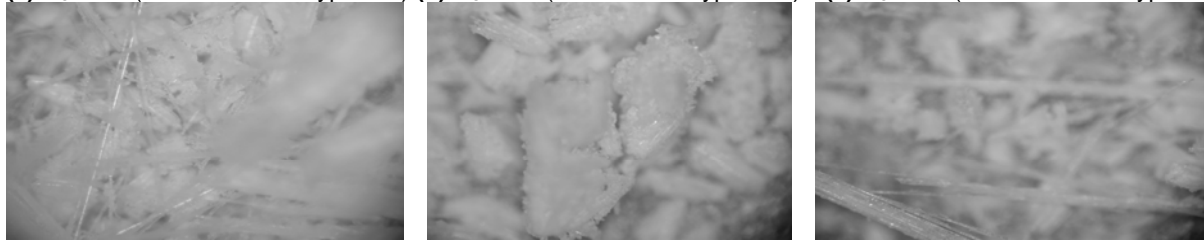


Fig. 23 Theoretical cutting forces : horizontal (F_x), transversal (F_y) and vertical (F_z) vs. rotating angles ($^\circ$) for chamfered and unchamfered main cutting edge K type carbide tool at $C_s=40^\circ$, $\alpha_{r1}(-30^\circ)$ and $\alpha_{r2}(30^\circ)$, $f=120\text{mm}/\text{min}$, $d=2.5$, and $V=285\text{m}/\text{min}$ (GFRP) respectively



(a) $C_s=20^\circ$ (unchamfered P type tool) **(b)** $C_s=20^\circ$ (chamfered P type tool) **(c)** $C_s=30^\circ$ (unchamfered P type tool)



(d) $C_s=30^\circ$ (chamfered P type tool) **(e)** $C_s=40^\circ$ (unchamfered P type tool) **(f)** $C_s=40^\circ$ (chamfered P type tool)

Fig 24 Shape of chips, unchamfered (a) (c) (e) and chamfered (b) (d) (f) of P carbide tool vs. C_s at $\alpha_{r1} = -30^\circ$, $\alpha_{r2} = 30^\circ$, $d=2.5$ mm, $f=120$ mm/min, and $V=285$ m/min (GFRP) respectively

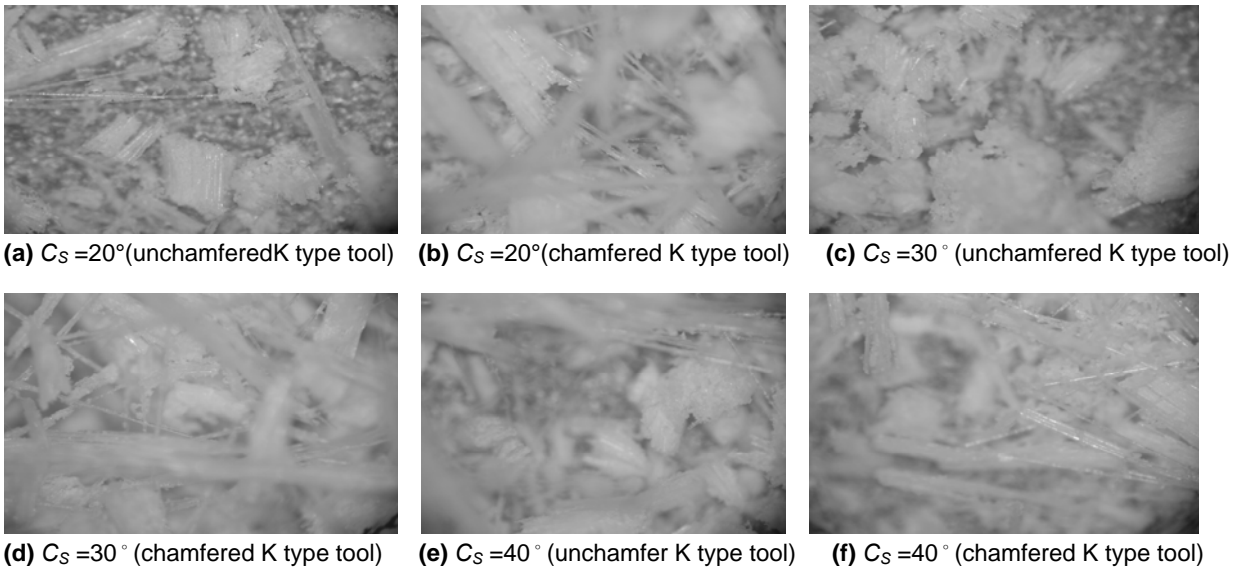
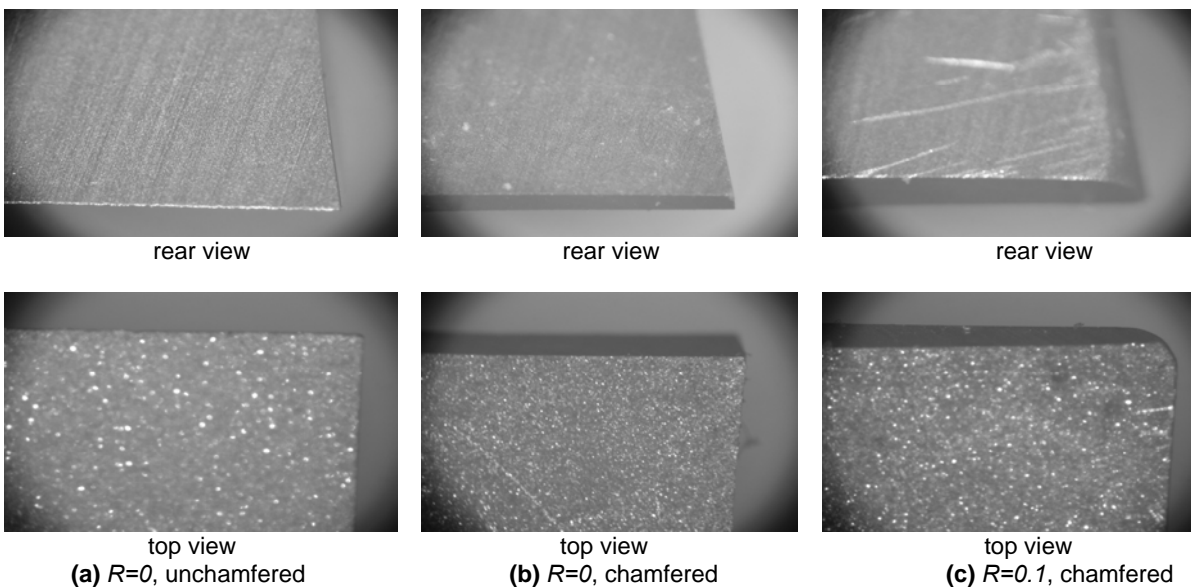
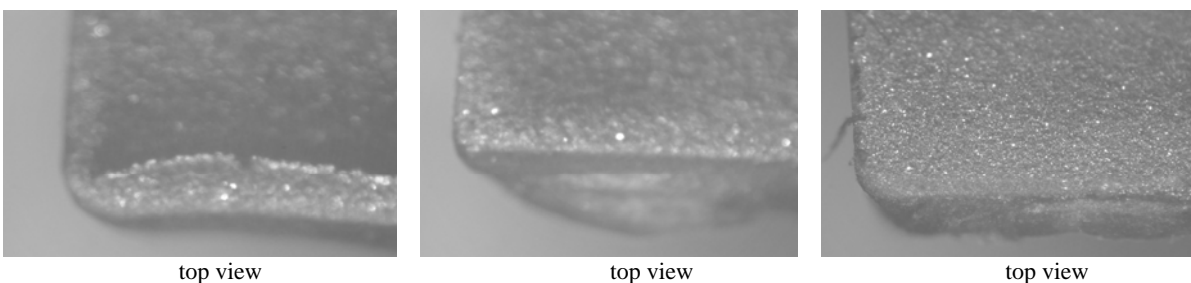
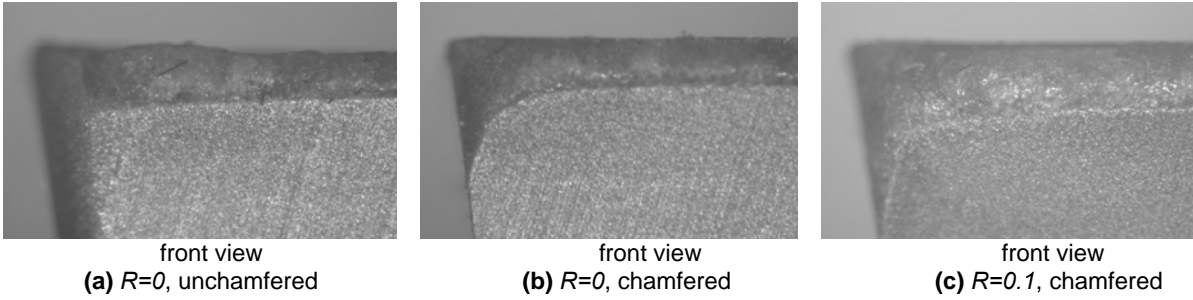


Fig 25 Shape of chips, unchamfered (a) (c) (e) and chamfered (b) (d) (f) of K carbide tool vs. C_s at $\alpha_{r1} = -30^\circ$, $\alpha_{r2} = 30^\circ$, $d=2.5$ mm, $f=120$ mm/min, and $V=285$ m/min (GFRP) respectively



Figs. 26 New of P type tool view (a), (b), and (c) with $C_s = 30^\circ$, and $\alpha_{r1} (\alpha_{r2}) = -30^\circ (30^\circ)$ respectively





Figs. 27 Worn of P type tool view (a), (b), (c), (d) and (e) with $C_s = 30^\circ$, and $\alpha_{r1} (\alpha_{r2}) = -30^\circ (30^\circ)$, at cutting time 10 min, $d=2.5\text{mm}$, $f=120\text{mm}/\text{min}$ and $V=285\text{m}/\text{min}$ respectively

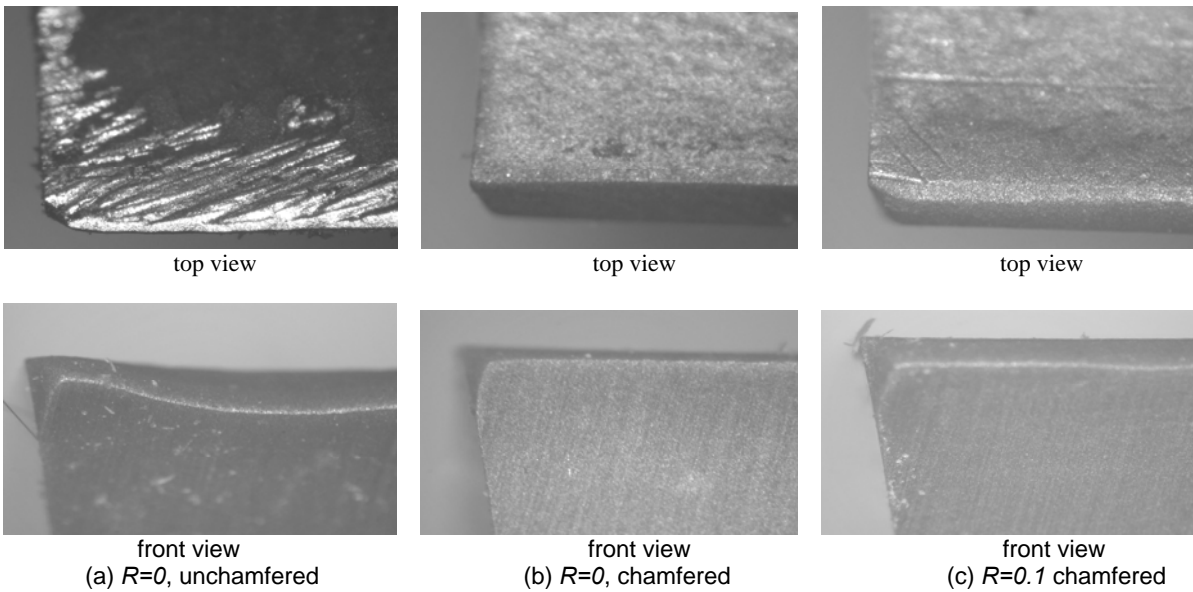


Fig. 28 Worn of K type tool view (a), (b), and (c) with $C_s = 30^\circ$, and $\alpha_{r1} (\alpha_{r2}) = -30^\circ (30^\circ)$, at cutting time 10 min, $d=2.5$, $f=120\text{mm}/\text{min}$ and $V=285\text{m}/\text{min}$ respectively

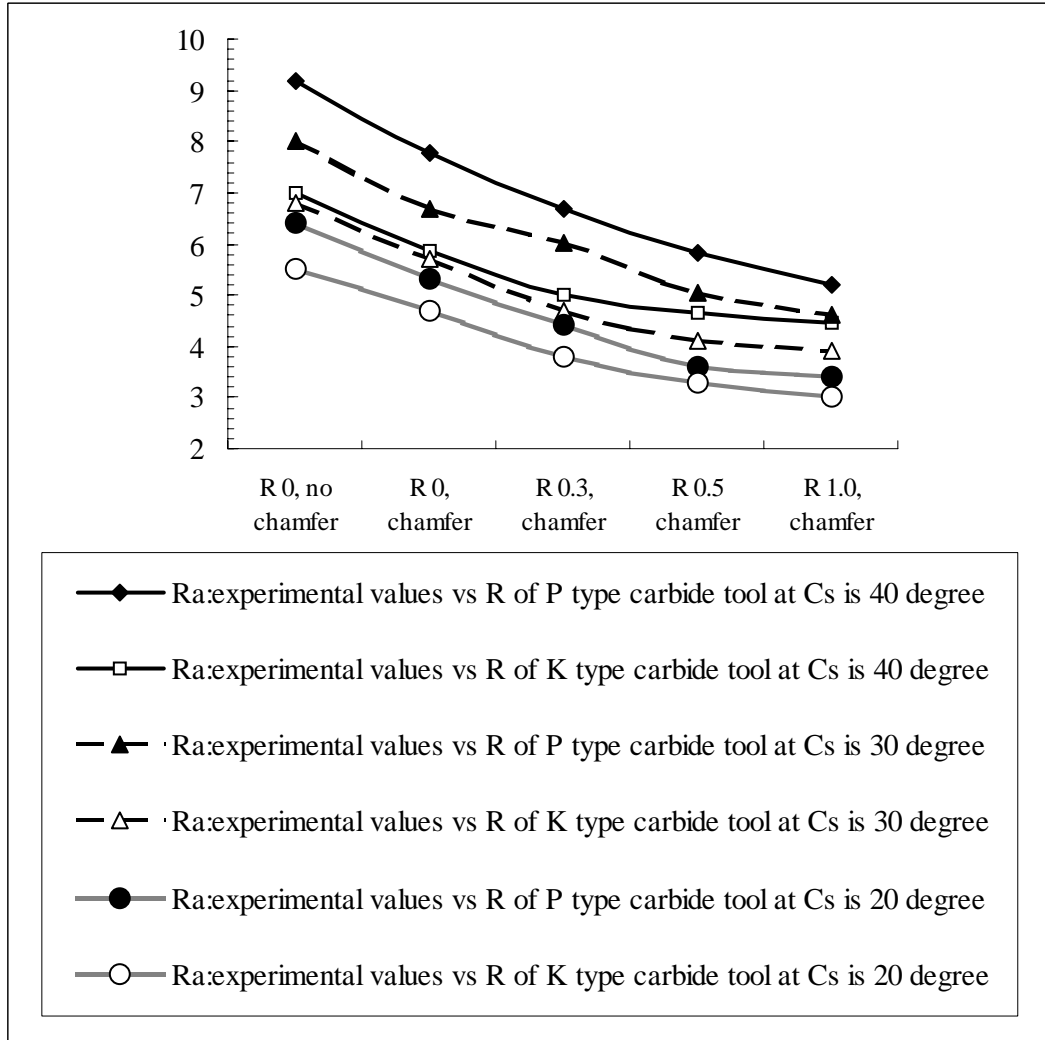


Fig. 29 Experimental surface roughness R_a vs. R , C_s of P and K type chamfered and unchamfered main cutting edge tools at α_{r1} (α_{r2}) = -30° (30°), $d=2.5$, $f=120\text{mm}/\text{min}$ and $V=285\text{m}/\text{min}$ respectively